

1

Earth-Abundant Metal-Based Nanomaterials for Electrochemical Water Splitting

Weiran Zheng, Yong Li, and Lawrence Yoon Suk Lee

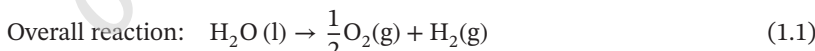
The Hong Kong Polytechnic University, Department of Applied Biology and Chemical Technology, Hung Hom, Kowloon, Hong Kong SAR, China

1.1 Electrochemical Water Splitting

Since the oil crisis in the 1970s and 1980s, hydrogen has been widely recognized to be an efficient and promising energy carrier for our future. Yet, as of 2019, about 95% of global hydrogen production relies on fossil fuels, emitting an excessive amount of carbon into the atmosphere [1]. Typically, for every ton of hydrogen produced by steam reforming of natural gas, around 9–12 tons of CO₂ is released and wasted [2, 3]. One of the most attractive options to produce hydrogen sustainably is to split water molecules using electrical energy generated by sustainable sources, such as wind, hydropower, nuclear energy, etc.

1.1.1 General Principle

In general, the electrochemical water splitting process requires passing electricity through two electrodes in water (Figure 1.1), where the oxidation occurs on the anode to generate oxygen (oxygen evolution reaction [OER]) and the reduction occurs on the cathode to produce hydrogen (hydrogen evolution reaction [HER]). The overall reaction can be simplified as Eq. (1.1):



Water splitting to hydrogen and oxygen is a thermodynamically uphill process, which requires a Gibbs free energy of $\Delta G^\circ = 237.22 \text{ kJ mol}^{-1}$ or enthalpy of $\Delta H^\circ = 285.84 \text{ kJ mol}^{-1}$ at standard conditions of temperature and pressure (298 K, 1 bar). When converting electrical energy to chemical energy, the equation of $\Delta G^\circ = nFE^\circ$ applies, where n is the number of transferred electrons (two electrons exchanged for the splitting of one water molecule), F is the Faraday's constant, and E° is the standard cell voltage required. Therefore, the thermodynamically required voltage for water splitting is 1.229 V. It should be noted that the voltage value depends on the temperature and water status. For example, the electrochemical

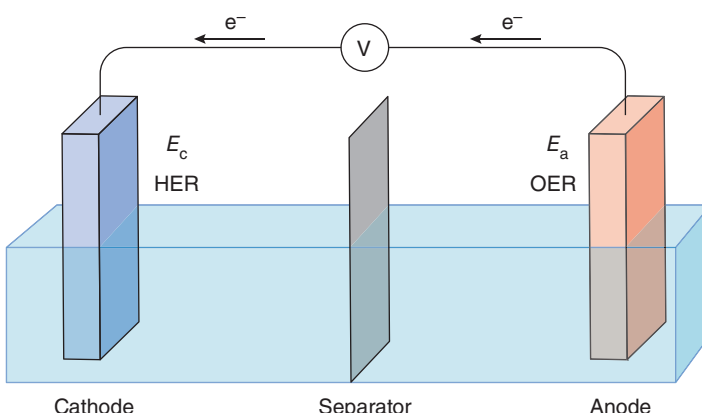


Figure 1.1 Simplified illustration of an electrolyzer for water splitting driven by a power source. The electrons travel through the external circuit and promote the HER at cathode and OER at the anode. A separator, often semipermeable membrane, is used for proton transfer and product separation.

dissociation of water vapor needs only 1.18 V. Since the electrolysis reaction is endothermic, if the reaction is performed without an external heat source, the extra voltage is needed to compensate the temperature factor in the enthalpy. In this case, the equation of $\Delta H^\circ = nFE^\circ$ applies, producing a value of 1.481 V at standard conditions, known as the thermoneutral potential.

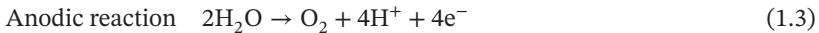
From an electrochemical perspective, the cell voltage needs to drive the two half-reactions at the electrodes:

$$E_{\text{cell}}^0 = E_{\text{c}}^0 - E_{\text{a}}^0$$

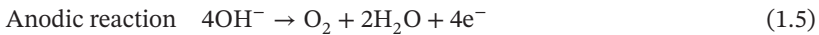
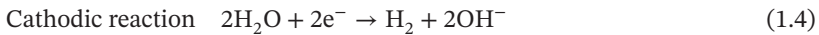
where E_{cell}^0 , E_{c}^0 , and E_{a}^0 represent the standard cell, cathodic, and anodic potential, respectively.

Although the overall reaction is irrelevant to electrolyte conditions, the two half-reactions follow two routes depending on the proton concentration of the electrolyte (Figure 1.2).

Under acidic conditions:



Under alkaline conditions:



The Nernst equation can express the thermodynamical potential to drive the anodic side in acidic conditions:

$$E_{\text{a}}^0 = E_{\text{H}_2\text{O}/\text{O}_2}^0 + \frac{RT}{nF} \ln \frac{\left(a_{\text{H}^+}^2\right) \left(f_{\text{O}_2}^{1/2}\right)}{a_{\text{H}_2\text{O}}}$$

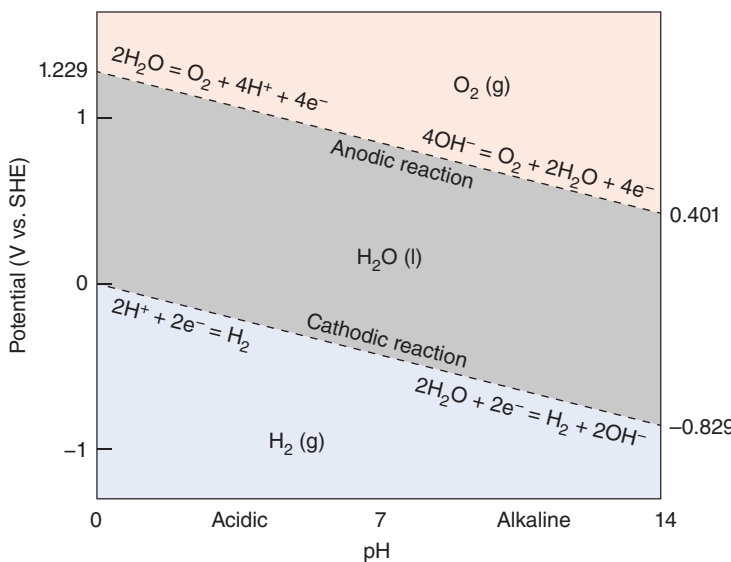


Figure 1.2 Pourbaix diagram (pH potential) of water under standard temperature and pressure (298 K, 1 bar).

where a_{H^+} and $a_{\text{H}_2\text{O}}$ are the activity of proton and water and f_{O_2} is the fugacity of oxygen in the anodic compartment. In a simplified case when the activity coefficient of the proton is unity and the water activity is the same at all concentration,

$$E_a^0 = 1.229 - 0.059 \text{ pH}$$

Similarly, for the cathodic side,

$$E_c^0 = E_{\text{H}_2/\text{H}^+}^0 + \frac{RT}{nF} \ln \frac{a_{\text{H}^+}^2}{f_{\text{H}_2}} \approx -0.059 \text{ pH}$$

Such expressions also apply for the alkaline conditions providing the electrolyte shares the same proton activity coefficient and water activity. Therefore, the standard potential for both anodic and cathodic reactions depends on pH.

1.1.2 Overpotential and Tafel Slope

Even if the desired potential is met, the reaction may not proceed, and extra potential (overpotential, η) beyond the thermodynamic value (E^0) is commonly required to overcome the reaction energy barriers caused by many factors:

$$\eta = E_{\text{applied}} - E^0$$

The causes of overpotential can be divided mainly into three categories: the resistance overpotential due to the ohmic losses in the electric circuit, the concentration overpotential caused by the concentration gradient in the double layer region of electrolyte, and the kinetic overpotential to drive the surface reaction [4]. Both electrode and electrolyte contribute to the ohmic loss. In a laboratory-scale

reaction, the potential drop due to ohmic loss is generally small and often not taken into account because the resistance of both electrode and electrolyte is negligible. However, industrial water electrolysis often suffers from the joule heat due to the ohmic resistance and large current. The concentration overpotential is the direct result of reactants consumption in the double-layer region near the electrode, therefore mainly controlled by the diffusion rate of the proton for water electrolysis. Conventionally, using electrolyte with highly acidic/alkaline conditions (extreme pH values) can offset such concentration effect and maximize efficiency. Accordingly, most researchers often employ electrolytes with pH = 1 or 14, and the current understanding of water splitting is also heavily based on the results from extreme pH levels. Industrial alkaline water electrolysis uses 20–40% NaOH or KOH aqueous solutions.

Like the concepts in heterogeneous catalysis, electrocatalysis also requires the reactants to be adsorbed first on the electrode to conduct further bond breaking and/or formation processes. Moreover, the electron transfer from/to the adsorbed reactants suffers resistance. As Eqs. (1.2)–(1.5) indicate, both anodic and cathodic processes demand an overpotential for proton/hydroxide and charge transfer for water splitting. The kinetic overpotential is referred to as the energy required to make the reactions proceed at appreciable rates. The faster the speed of water splitting is (measured as normalized charge flowing in the circuit, or current density), the higher overpotential must be supplied. The kinetic parameter used to describe such dependency is the Tafel slope (unit: mV dec^{-1}), defined as the overpotential needed to increase the current density by a factor of 10.

Due to the existence of overpotential, the energy efficiency of an electrolysis process is not 100%. When considering the efficiency in the lab, the Faradaic efficiency (ratio of the electrons used for hydrogen production vs. the total charge passed) is commonly used. The experimental value may approach 100% but is always lower than 100% because of some parasitic processes such as the conversion of the electrocatalyst. The energy loss due to resistance, however, cannot be revealed by the Faradaic efficiency. Industrial water electrolyzers often use a more practical way to evaluate the energy efficiency of water splitting by dividing the energy available from the produced hydrogen by the total energy consumed by the cell. Such value reflects the energy loss due to the overpotentials and uncovers the commercial viability of the system.

To achieve the highest energy efficiency, the energy spent on overcoming the extra barriers needs to be minimized. The role of electrocatalysts is to reduce the kinetic overpotential as much as possible. Over the past decades, electrochemists have been working on finding the best electrocatalysts for both HER and OER under acidic and alkaline conditions. Two indicators are generally used in literature for comparison: the overpotential to achieve a current density of 10 mA cm^{-2} and the Tafel slope within a specific current range.

1.1.3 Current Techniques

Two main techniques have been commercialized for electrochemical water splitting, including alkaline electrolysis and proton exchange membrane (PEM) electrolysis. The alkaline electrolysis follows the alkaline pathway described in reactions

(1.4) and (1.5) and remains the dominating commercial approach. Both cathode and anode are often made of nickel-based materials, and the separator is a polymer that allows hydroxide ions and water molecules to pass. The PEM electrolysis that has emerged more recently follows the acidic pathway (reactions (1.2) and (1.3)) with a PEM separator placed between the electrodes to allow proton transfer. Considering the highly acidic conditions, the electrocatalysts engaged in the PEM electrolysis need to be stable under the operating environment, leaving far less choices comparing with alkaline electrolysis. The current state-of-the-art catalysts in PEM electrolysis is platinum and iridium/ruthenium oxides for HER and OER, respectively.

Although the alkaline electrolysis is more technologically mature and relatively cost-effective compared with the PEM electrolysis, it has some drawbacks such as low current density, low partial load range, low operational pressures, and hydrogen crossover through the separator. The high efficiency of PEM electrolysis, on the other hand, cannot redeem the expensive noble metal-based electrode materials. Based on the calculation by Chatzitakis and coworkers [5] a typical PEM electrolyzer requires 0.4 mg cm^{-2} Pt on the cathode and 1.54 mg cm^{-2} Ir and 0.54 mg cm^{-2} Ru on the anode, respectively. Yet, for a power density of 1.18 W cm^{-2} , 1.5, 180, and 12 years of the annual production of Pt, Ir, and Ru, respectively, are demanded.

To further improve both techniques, the development of electrocatalyst for alkaline water electrolysis needs to focus on materials bearing high current at relatively low overpotential. As to the PEM electrolysis, finding suitable alternatives that are stable under extremely acidic conditions while showing similar activities to the noble metal-based ones is essential.

1.2 Earth-Abundant Metallic Nanomaterials

The key to large-scale commercialization is to lower the cost of water electrolysis systems. Apart from increasing the activity of noble metal atoms, using earth-abundant metal-based materials as the electrocatalysts is generally appreciated by the research community. The elements currently of particular interest are nickel (Ni), cobalt (Co), iron (Fe), manganese (Mn), titanium (Ti), vanadium (V), and molybdenum (Mo), as shown in Figure 1.3.

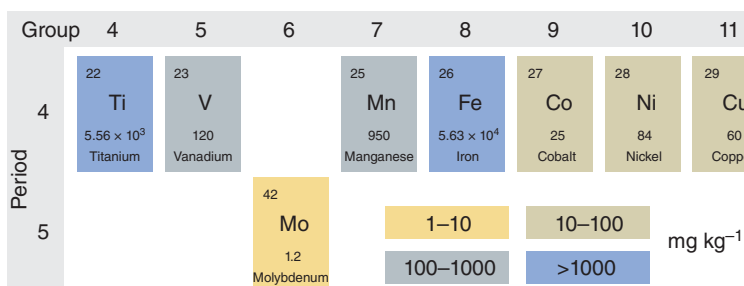


Figure 1.3 Earth-abundant metals that are currently used for water electrolysis and their relative positions in the periodic table. Their abundance in Earth's crust [6] is shown in the unit of mg kg^{-1} .

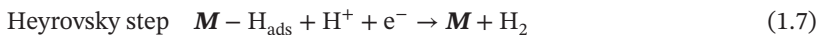
In the following contents, the current research progress of individual metal-based materials in different forms (metal, metal oxide, metal hydroxide, metal chalcogenide, metal sulfide, etc.) will be introduced based on their application: HER and OER. In many cases, the electrocatalytic materials involve more than one metal element. For clarity, their descriptions are listed under the major element responsible for active sites.

1.2.1 Hydrogen Evolution Reaction (HER)

1.2.1.1 Mechanism

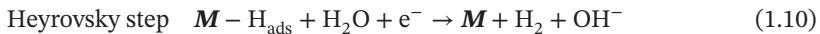
The well-established mechanism for HER (heavily based on Pt electrode) can be generally described as the electrochemical hydrogen adsorption followed by hydrogen desorption reactions and/or chemical desorption [7].

Under acidic conditions (\mathbf{M} represents the HER active sites on electrocatalysts):



In acidic media, the proton first gains an electron at the active site to form $\mathbf{M} - \text{H}_{\text{ads}}$ intermediate (reaction (1.6)). In alkaline media, instead of proton adsorption, the water molecule is involved in the elemental reactions (reactions (1.9) and (1.10)).

Under alkaline conditions:



Most HER catalytic systems adopt either the Volmer–Heyrovsky or Volmer–Tafel pathway for mechanism understanding. An approximate way to determine the mechanism is to use the Tafel slope, derived from the HER polarization curve. If the Volmer step is the rate-determining step (RDS), the slope is 120 mV dec^{-1} , and when Heyrovsky and Tafel steps are the RDS, the Tafel slopes of 40 and 30 mV dec^{-1} result, respectively.

Both the bonding strength of the $\mathbf{M} - \text{H}_{\text{ads}}$ intermediate and the free energy of hydrogen adsorption (ΔG_{H}) on the cathode can be used to describe the interaction between the hydrogen atom and active sites. When plotting the two descriptors with the experimentally measured exchange current densities from polycrystalline metal electrodes, a typical volcano relationship emerges (Figure 1.4), demonstrating the so-called Sabatier principle. Neither too strong nor too weak bonding benefits the HER. Only a moderate value of ΔG_{H} helps the hydrogen gas discharge following the Heyrovsky step (reaction (1.7)) and/or Tafel step (reaction (1.8)).

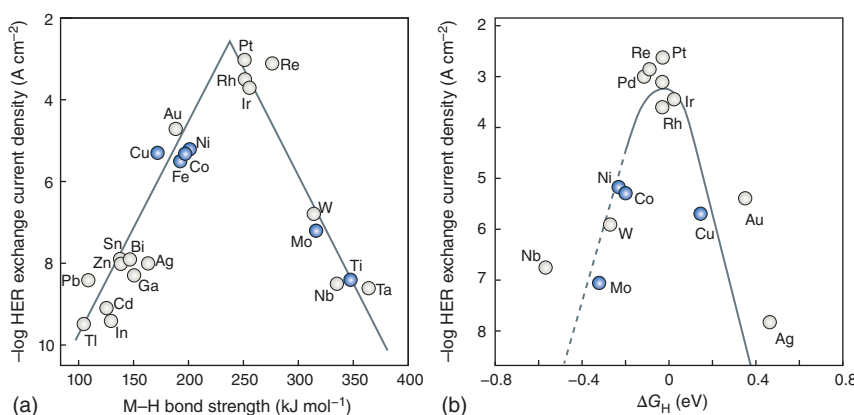


Figure 1.4 HER volcano plots with measured exchange current density of polycrystalline metal vs. (a) the energy of the intermediate metal–hydrogen bond formation. Source: Trasatti [8]. Reproduced with permission of Elsevier. (b) The calculated free energy of H adsorption. Source: Skúlason et al. [9]. Reproduced with permission of American Chemical Society. The earth-abundant metallic elements are marked in blue.

1.2.1.2 Metal (M^0) Nanoparticles

The metallic form of earth-abundant metals usually shows limited HER activity and stability in both acidic and alkaline media [10, 11]. Major efforts have been devoted to increasing metal sites' activity and stability. Decreasing the size of metals to the nanoscale is a proven strategy to alter the electronic properties of metal sites (Figure 1.5) [13, 14]. The high surface energy of metallic nanoparticles, however, renders them unstable. The most straightforward solution is to stabilize the nanoparticles using supports, which can be structurally engineered to affect the electronic properties of the metal nanoparticles to benefit HER activity.

One typical example is Co nanoparticles. A recent report shows that Co nanoparticles encapsulated in nitrogen-enriched carbon material can deliver a reasonable overpotential (at a current density of 10 mA cm^{-2} , or η_{10}) of 265 mV in acid and 337 mV in base [15]. It was claimed that the synergistic effects between Co nanoparticles and N-doped carbon can significantly enhance the activity of Co sites.

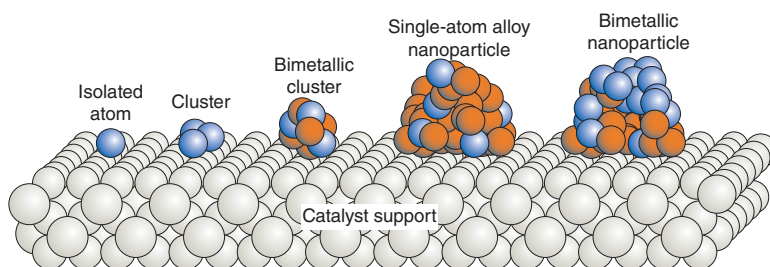


Figure 1.5 Illustration of various forms of metallic electrocatalysts, from isolated metal atoms to bimetallic nanoparticles supported on conventional solid carriers. Source: Liu and Corma [12]. Reproduced with permission of Springer Nature.

Similarly, by decorating TiO_2 nanoparticles on the surface of Co nanostructure, the hydrogen adsorption free energy at the material junction can be optimized to achieve a η_{10} of 229 mV in 1.0 M KOH, which is highly enhanced compared with 356 mV using unmodified Co nanomaterial [16]. Similar strategies are frequently applied to other earth-abundant metal nanoparticles. The commonly used supports include the following: *for Co nanoparticles*, carbon-nanotube (CNT)-grafted graphene sheet [17]; *for Ni nanoparticles*, nitrogen-doped graphitized carbon driven by Ni(II)-dimeric complex [18], nitrogen-doped CNT [19, 20], carbon fiber cloth [21], hydrophilic graphene [22], and graphene [23]; and *for Fe nanoparticles*, carbon shell encapsulation [24] and nitrogen-doped carbon [25]. Notably, the formation of metal–N local environment has been proven an efficient method to promote the HER activity of metal nanoparticles. Meanwhile, the employment of support is essential for small metal clusters, especially for the stability during reactions.

Another commonly employed approach is to change the shape of the metal nanoparticle, which exposes highly active sites or desired surface features, such as corners and edges, as demonstrated in the HER study of Cu nanoparticles with different shape [26]. However, the tunability of the single element metal nanoparticle is limited by the intrinsic properties of the element.

Involving two or more earth-abundant metals for the construction of HER electrocatalyst is more popular as more flexibility is possible. The introduction of another/multiple metal(s) into a hosting metal lattice can modify the original electronic structure via strain effect and the bonding strength of adsorbed hydrogen atoms. By combining metals on opposite slopes of the volcano-type plots (Figure 1.4), new materials systems are proposed to produce suitable intermediate hydrogen binding energy and improved HER activity. For instance, although both Cu and Ti are poor HER electrocatalysts, their combination allows the creation of Cu–Cu–Ti hollow sites with hydrogen binding energy close to that of Pt [27]. The various combinations of metals, tunable ratios, and multiple morphologies (core–shell, alloy, etc.) allow nearly infinite possibility to be explored. Some of the most exciting systems include Cu–Ti [27], Cu–Co [28], Cu–Ni [29], Ni–Mo [30], Fe–Co [31], and Ni–Co–Fe [32]. Depending on the mechanism, one element may serve as the primary active sites for HER and the heteroatoms can aid either proton adsorption or electron transfer [30]. In other cases, the active sites are identified as the hollow sites surrounded by different atoms [27].

1.2.1.3 Metal (M^0) Single-Atom Catalysts

Decreasing the size of metal nanoparticle to the extreme leads to the development of single-atom electrocatalysts (Figure 1.5). Since its first appearance in 2011 [33], the concept of using single-atom catalysts (SACs) has been drawing wide attention due to the maximum atomic utilization close to 100%. The initial intention for SACs as HER catalysts is to minimize the Pt loading without sacrificing HER activity [34]. However, when the single atoms are isolated and supported on different materials, their properties change significantly from their bulk nanoparticles [12]. In addition to the noble metals, several earth-abundant metals, including Co [35], Fe [36], Ni [36, 37], Mo [38], and W [39], have shown unexpected HER activities (selected

Table 1.1 Selected earth-abundant metal single-atom electrocatalyst for HER.

Entry	Metal	Coordination environment	Overpotential at 10 mA cm^{-2} (mV)	Tafel slope (mV dec $^{-1}$)	Electrolyte	References
1	Co	N-doped graphene	147	82	0.5 M H_2SO_4	[35]
2	Co	Phosphorized carbon nitride	89	38	1 M KOH	[40]
3	Fe	Graphdiyne	66	37.8	0.5 M H_2SO_4	[36]
4	Fe	N-doped carbon	111	86.1	1 M KOH	[41]
5	Ni	Graphdiyne	88	45.8	0.5 M H_2SO_4	[36]
6	Ni	Graphene	180	45	0.5 M H_2SO_4	[37]
7	Mo	N-doped carbon	132	90	0.1 KOH	[42]
8	W	N-doped carbon	85	53	0.1 KOH	[39]
9	W, Mo	N-doped graphene	24	30	0.5 M H_2SO_4	[43]
10	W, Mo	N-doped graphene	67	45	1 M KOH	[43]

results shown in Table 1.1). Moreover, a series of literature reviews on the topic of SACs were published, covering from their preparation methods to applications [44–47].

The synthesis of SACs with robust structures and reasonable performance is the major challenge since the highly active single atoms tend to aggregate during the catalytic reaction and result in a lower activity. With the advance of experimental techniques, current strategies include wet chemistry method, atomic layer deposition (ALD), template-driven decomposition (mainly metal–organic frameworks), and electrochemical deposition [47, 48]. Typically, such methods produce nanocomposites with isolated metal atoms decorated on a support to prevent migration and aggregation of single atoms. Therefore, the nature of the support and the metal coordination sites can impact the activity of SACs for HER significantly. As revealed by Gao et al. using *ab initio* calculation, the hydrogen bonding free energy on the same metal species at different coordination sites of graphene varies largely to show versatile HER activities [49] (Figure 1.6).

Carbon supports, including graphene and CNTs, are the most popular choice for SACs. Fan et al. demonstrated a Ni–C electrocatalyst with carbon nanoparticles dotted with isolated nickel atoms. Under acidic conditions, the Ni–C electrocatalyst exhibited a performance comparable with the commercial Pt/C electrocatalyst even when operating at a current density of 100 mA cm^{-2} . Remarkably, no significant activity loss was observed over 25 hours of continuous operation [50]. Density function theory (DFT) calculations study by He et al. suggested that Fe, Co, Ni, and V supported on carbon are all promising SACs for HER. Especially, V atom on carbon shows a Gibbs free energy of -0.01 eV of hydrogen adsorption, which is close to that of Pt [51].

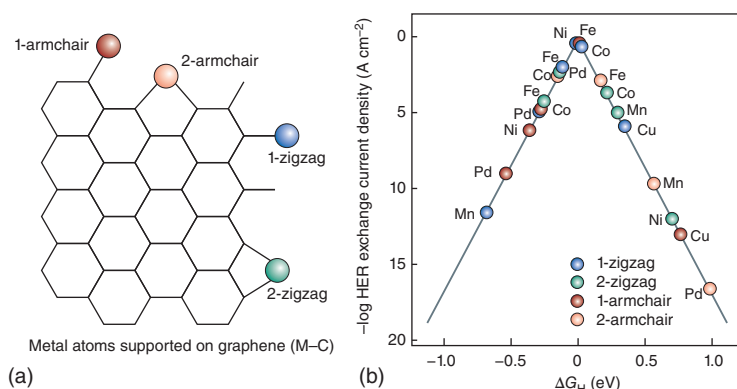


Figure 1.6 (a) Model of metal atoms supported on graphene via metal–carbon coordination. (b) Calculated volcano curve of exchange current density as the function of Gibbs free energy of hydrogen adsorption on coordinated metal sites. Source: Gao et al. [49]. Reproduced with permission of Royal Society of Chemistry.

Functionalization/doping of the carbon supports with other non-metallic atoms allows fine-tuning of the metal sites' properties. One of the most commonly reported cases is nitrogen-doped carbon materials. The N atoms can form strong bondings with the metal sites for better stability and assist electron transfer to the d orbitals of the metal sites [39, 42, 52]. Cao et al. reported a SAC system where Co atoms were anchored by N atoms in graphitic carbon nitride to form $\text{Co}-\text{N}_4$ sites (Co atoms are covalently grafted by four N atoms) [53]. The coordinated nitrogen sites can donate electrons to the Co sites to lower the formation barrier of $\text{Co}-\text{H}$. Later, by using *operando* spectroscopy, they revealed the formation of a high-valence $\text{HO}-\text{Co}-\text{N}$ environment from $\text{Co}-\text{N}_4$ sites in the alkaline reaction conditions, which enabled the water adsorption to assist water splitting (Eq. (1.9)) [40]. With a low Tafel slope of 52 mV dec^{-1} , a Volmer–Heyrovsky mechanism was proposed (Figure 1.7).

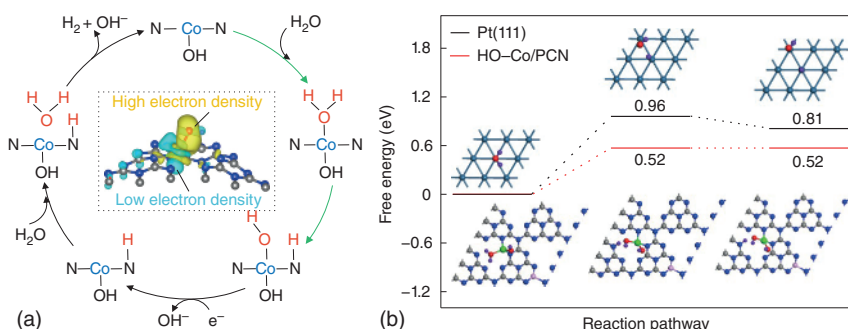


Figure 1.7 (a) Alkaline HER mechanism on $\text{Co}-\text{N}$ SAC. Inset shows the electron density at different regions of the $\text{HO}-\text{Co}-\text{N}$ environment. (b) Calculated adsorption energies of H_2O and H on the surface of $\text{HO}-\text{Co}-\text{N}$ and $\text{Pt}(111)$. Source: Cao et al. [40]. Reproduced with permission of Springer Nature.

For most SACs, the metal active sites are exclusively responsible for hydrogen production. As a result, higher loading of metal sites always means higher overall activity at the same surface area of the catalyst, which remains a challenge nowadays. Current state-of-the-art systems typically have metal loading <3 wt%. Despite the high activity of individual atoms, their overall performance is not compatible with commercial ones. The surface engineering of the support to accommodate more metal atoms, therefore, is the key to promote SACs for further large-scale HER applications. Inorganic supports beyond carbon, such as boron monolayer [54] and boron nitride [55], are under active investigations. More suitable SAC supports are expected to emerge in the near future.

Other than support engineering, engaging more than one metal atoms can offer a more optimized environment for HER, as demonstrated by Yang et al. who demonstrated that W and Mo dual-atom catalyst is a better HER catalyst than W-/Mo-SACs [43].

1.2.1.4 Metal Phosphides

Transition metal phosphides (TMPs, e.g. CoP, Ni_5P_4 , MoP, Cu_3P , and FeP) have attracted increasing attention for HER owing to their good hydrogen adsorption property. As the P atom possesses a high electronegativity, the transition metal sites (TM) are usually positively charged in TMPs, and the TM—P bonds can serve as a proton acceptor to promote HER activity [56]. Based on previous reports, the increased P content in TMPs can improve the HER activity. For examples, nickel phosphide and molybdenum phosphide exhibit HER activity trend of $\text{Ni}_5\text{P}_4 > \text{Ni}_2\text{P} > \text{Ni}_{12}\text{P}_5$ [57] and $\text{MoP} > \text{Mo}_3\text{P} > \text{Mo}$ [58], respectively. In contrast, the excessive P content may reduce the performance owing to the reduced electronic conductivity. Therefore, the P content in TMPs should be adjusted to optimize the activity. To further improve the HER activity, metal doping, non-metal doping, hybridization, and coupling with carbon materials have been adopted.

Up to date, various metallic elements, such as Fe, Co, Zn, Mn, and Mo, have been doped into TMPs to improve HER activity (Figure 1.8) [59, 60]. Guan et al. synthesized hollow Mo-doped CoP nanoarrays on carbon cloth by low-temperature annealing with NaH_2PO_2 [61]. The Mo-doped CoP showed a superior HER activity with a low overpotential of 40 mV in 1.0 M KOH, and the P sites were considered as the HER active sites. According to the DFT calculations, the hydrogen adsorption energy on the P sites was only 0.07 eV, which is close to zero and thus enhanced the HER activity. Similarly, Mn-doped Ni_2P also exhibited an excellent HER activity with an overpotential of 84 and 122 mV in 0.5 M H_2SO_4 and 1 M KOH, respectively [62]. The Mn dopants were claimed to provide electrons to adjacent Ni atoms and weaken the Ni— H_{ad} bonds to improve the HER activity. Besides, Fe and Co were doped to Ni_2P , and Zn was doped to CoP for HER enhancement [63, 64].

The N and S elements were widely reported as the non-metal dopants to improve the HER activity of TMPs. Zhang's group reported N-doped CoP as an excellent HER catalyst [65]. Because of the higher electronegativity of N than P, the positively charged Co could enhance the Co–Co interaction and lower the d-band. Therefore, the Co— H_{ad} bonds were weakened with an optimized hydrogen adsorption energy

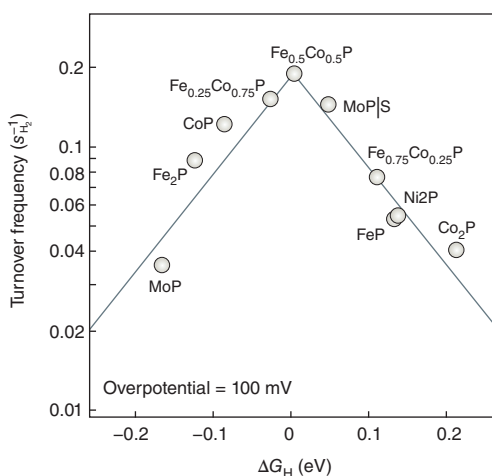


Figure 1.8 HER volcano plot of TMPs showing the average H_2 turnover frequency at an overpotential of 100 mV as a function of ΔG_{H} . Source: Kibsgaard et al. [59]. Reproduced with permission of Royal Society of Chemistry.

of -0.14 eV, which is higher than the undoped CoP (-0.52 eV) and closer to zero. Recently, S-doped Ni_5P_4 nanoplate arrays and S-doped MoP nanoporous layers were also reported as efficient HER catalysts [66, 67].

Hybridizing the TMPs with other compositions can construct an active interface and induce a synergistic effect, beneficial for HER enhancement. The TMPs hybridized with metal oxides [68, 69], hydroxides [70], sulfides [71], or even another TMP [72] were reported. Luo et al. prepared Mo-doped $\text{Ni}_3\text{S}_2/\text{Ni}_x\text{P}_y$ hollow nanorods that delivered 10 mA cm^{-2} at an overpotential of 109 mV for HER in 1.0 M KOH [73]. The heterostructure not only enhanced the adsorption of the water molecule but also decreased the value of hydrogen adsorption energy to improve HER activity.

Coupling with carbon materials is another viable strategy to improve HER activity by enhancing the electronic conductivity and number of active sites. With this respect, carbon materials have gained large attention due to their high conductivity, structural stability, and corrosion resistance. The large surface area of carbon materials can also restrain the aggregation of nanosized TMPs. For examples, MoP nanoparticles decorated on CNTs or anchored on reduced graphene oxide (RGO) exhibited suitable HER activities in both acidic and basic media [74, 75]. Other TMPs were also reported to be modified on carbon materials, such as CoP/N,P co-doped carbon frameworks [76] and CoP/CNT [77], for enhanced HER activities. TMPs were also encapsulated by carbon to form core-shell structures, for example, $\text{Co}_x\text{P}@\text{NC}$ [78] and $\text{Ni}_2\text{P}@\text{graphene}$ [79]. Unlike the usual TMPs exposed to substrates, the encapsulated TMPs cannot provide active sites for HER, and it is generally considered that HER takes place on the exposed carbon sites or N dopants in the carbon shell.

1.2.1.5 Metal Chalcogenides

Transition metal chalcogenides (TMCs) can be represented with a formula MX_2 , where $\text{M} = \text{Mo, W, or V}$ and $\text{X} = \text{S or Se}$. It is well accepted that the two-dimensional (2D) layered TMCs exhibit three types of structures: 1T (single $\text{X}-\text{M}-\text{X}$ layer),

2H, and 3R (several X–M–X layers). The 1T phase predominantly consists of edge-sharing MX_6 octahedra, while 2H and 3R polymorphs consist of edge-sharing MX_6 trigonal prisms [80]. Among them, the 1T and 2H phases are commonly employed in water splitting electrocatalysis.

MoS_2 , first investigated by Nørskov's group in 2005 [81], is considered as one of the promising HER catalysts. Owing to the unique 2D layered structure, MoS_2 has two distinct types of surfaces: (i) the S sites located on the basal plane and (ii) the exposed Mo and S sites on the edge plane [82]. Many experimental studies have attributed the HER activity of MoS_2 to its edge sites [83, 84]. To further improve the HER activity of MoS_2 , abundant edge active sites were created by synthesizing nanostructures. Cui's group reported MoS_2 with vertically aligned layers to maximize the exposure of active edge sites and found that the HER activity could be modulated by adjusting the density of the exposed edge sites [85]. Other nanostructures, such as MoS_2 nanoparticles, core–shell MoO_3 – MoS_2 nanowires, and molecular clusters, have also been reported [86, 87].

It was reported that the phase of MoS_2 can affect HER activity: 1T MoS_2 exhibits a higher catalytic activity than 2H MoS_2 . The 2H phase is generally considered as an inactive toward HER catalysis because of semiconductive property that inhibits the charge transfer. On the other hand, the 1T phase has a good hydrogen adsorption property and conductivity to improve the charge transfer kinetics [88]. Voiry et al. prepared metallic 1T phase from 2H MoS_2 by a solvent-free intercalation method, which showed an enhanced HER activity [89]. Meanwhile, when a small amount of CNTs was modified on the surface of 2H MoS_2 phase, the catalytic activity was also improved, confirming that the importance of conductivity for HER. Aiming to enhance the conductivity, the integration of MoS_2 and carbon materials was recently reported for HER enhancement, for example, MoS_2 /Co–N-doped carbon nanocages [90] and CNTs/ MoS_2 nanoflake [91].

The first-row transition metals (Ni, Fe, Co) are also useful for TMCs to form highly active HER catalysts. The crystalline structures of MX_2 (Ni, Fe, Co) are slightly different from MoS_2 , which consists of corner-sharing or edge-sharing MX_6 octahedra that forms pyrite or marcasite structures, respectively [92]. Among the nickel chalcogenides, NiS , NiS_2 , and Ni_3S_2 have been reported for highly active HER activities. Jiang et al. found that Ni_3S_2 exhibited better HER activity than NiS and NiS_2 , owing to the larger active surface area and higher intrinsic conductivity [93]. However, the bonds of adsorbed hydrogen intermediates on Ni_3S_2 are still too strong, making it challenging to generate H_2 . To optimize the hydrogen adsorption property, interface engineering has been widely adopted by hybridizing Ni_3S_2 with other compositions. Cu nanodots were decorated on Ni_3S_2 nanotubes by Feng et al. to work as electrons donators [94]. The positively charged Cu in $\text{Cu}/\text{Ni}_3\text{S}_2$ optimized the hydrogen adsorption energy and thus facilitated the water dissociation. Based on the S–H_{ad} peak observed from the *in situ* Raman spectra, the authors claimed that S sites were responsible for HER activity. An Ni– Ni_3S_2 hybrid structure was also reported to improve the HER activity [95]. According to the first-principles calculations, the metallic Ni is believed to work as the active material for HER, and the Ni/ Ni_3S_2 interface facilitates the water adsorption and dissociation. Ni selenides are another

type of nickel chalcogenides and have been also reported for HER activity recently. Anantharaj et al. compared different structures of Ni selenides by controlling the ratio of Ni to Se, whose HER activity followed the order of $\text{NiSe}_2 > \text{Ni}_3\text{Se}_4 > \text{Ni}_{0.85}\text{Se}$ [96]. The HER activity was improved by increasing the content of Se, indicating that Se sites might be responsible for the proton adsorption [97]. Wang et al. synthesized Se-enriched NiSe_2 and confirmed that the hydrogen adsorption energy on Se sites is much lower than that of Ni sites, which endowed an excellent HER activity with an ultralow Tafel slope of 32 mV dec^{-1} [98].

Cobalt chalcogenides have attracted attention as efficient HER catalysts of low overpotential and small Tafel slope. The HER activity of cobalt chalcogenides (CoS_2 and CoSe_2) can be further improved by doping heteroatoms. Ternary pyrite-type CoPS nanostructures (film, nanowires, and nanoplates) were synthesized by Jin's group and showed excellent HER activities [99]. Compared with CoS_2 , the existence of adjacent P—H_{ad} bonds in CoPS reduced the oxidation state of Co^{3+} to Co^{2+} . The Co^{2+} sites were believed to optimize hydrogen adsorption sites and would be oxidized back to Co^{3+} after hydrogen adsorption. Dutta et al. also synthesized CoSSe microspheres to improve the HER activity of CoS_2 by optimizing the hydrogen adsorption energy of Co sites [100]. Ni atoms were doped to CoSe_2 to generate $\text{Ni}_{0.33}\text{Co}_{0.67}\text{Se}_2$ nanostructure by Xia et al. [101]. The $\text{Ni}_{0.33}\text{Co}_{0.67}\text{Se}_2$ exhibited an excellent HER activity with an overpotential of 65 mV in $0.5 \text{ M H}_2\text{SO}_4$, which was attributed to the improved conductivity and increased active surface area.

There are only a few reports on the HER activity of Fe chalcogenides, owing to the unfavorable intrinsic activity of Fe. Recently, Jasion et al. tried to improve the HER activity of FeS_2 by controlling the ratio of Fe to S in its 0, 1, and 2D nanostructures (cubes, wires, and disks, respectively) [102]. Among them, the 2D FeS_2 exhibited excellent HER activity and stability. Inspired by this work, Miao et al. synthesized mesoporous FeS_2 nanoparticles containing exposed (210) facets [103], which demonstrated excellent HER activity in alkaline media. Compared with the (100) surface, a higher water adsorption energy and a lower activation barrier energy were obtained on the (210) surface, resulting in the promotion of HER activity. Similarly, FeSe_2 is also known to have an inactive HER activity. Even though coupling Co or Mo could improve the performance, the prepared $\text{Fe}_x\text{Co}_{1-x}\text{Se}_2$ still suffered from an insufficient catalytic activity, much lower than that of Pt. [104] The incorporation of Mo caused the phase separation to form 1T $\text{MoSe}_2/\text{FeSe}_2$ heterostructure, and the improved HER activity might be attributed to the 1T MoSe_2 phase near the interface [105].

1.2.1.6 Metal Nitrides

Transition metal nitrides have been also reported as earth-abundant catalysts for HER. A nitrogen-rich 2D Mo_5N_6 nanosheet was synthesized by Qiao's group and demonstrated superior HER activity [106]. The higher valence state of Mo (+4) in Mo_5N_6 than that of MoN (+3) facilitated the water dissociation in alkaline media and induced the downshift of the d-band center of Mo, which resulted in optimizing the hydrogen adsorption energy. Liu et al. introduced N vacancies into Ni_3N to further improve HER activity and achieved an ultralow overpotential of 55 mV in

1.0 M KOH media [107]. The N vacancies enriched in $\text{Ni}_3\text{N}_{1-x}$ were also beneficial for hydrogen adsorption due to the downshift of d-band center. Similarly, Chen et al. doped V atoms into Co_4N to tailor the d-band center of V- Co_4N , which also exhibited an excellent HER activity closed to the Pt/C catalyst [108]. Besides, constructing an active interface in nitride heterostructures was also reported to improve the HER activity, for instances, $\text{Ni}/\text{Co}_2\text{N}$ [109] and $\text{Mo}_2\text{N}/\text{CeO}_2$ [110].

1.2.1.7 Metal Carbides

The HER catalysts based on transition metal carbides are mainly focus on molybdenum carbides, including α - MoC_{1-x} , β - Mo_2C , and η - MoC [111]. Recent works showed that the catalytic performance of molybdenum carbides can be further improved by doping heteroatoms or constructing an interface. Ma et al. claimed that the d-band center and the strength of Mo—H bonds of β - Mo_2C spheres could be modulated by doping Co atoms [112]. Such modulated Co- Mo_2C exhibited a low onset potential of 27 mV. Huang et al. compared the transition metal (Fe, Co, Ni, and Mn)-modified Mo_2C and found that the Fe- Mo_2C exhibited the best HER activity with an overpotential of 65 mV in 1.0 M KOH media, owing to the optimized hydrogen adsorption energy [113]. The α - MoC_{1-x} decorated with ultrafine Pt nanoparticles was reported to exhibit a higher intrinsic HER performance than commercial Pt/C [114].

1.2.1.8 Metal Oxides/(Oxy)hydroxides

The pristine transition metal oxides (NiO , Co_3O_4 , TiO_2 , MoO_2 , MnO_2 , Fe_2O_3 , V_2O_5 , etc.) are normally considered to be inactive HER catalysts owing to their semiconductive property and unfavorable hydrogen adsorption and desorption processes [115]. To improve their HER activities, some strategies have been widely discussed, such as morphology engineering, oxygen vacancies (OVs), and heteroatoms doping.

Morphology engineering is an effective way to create active sites on the surface of catalysts. The common strategy is to synthesize nanoscale metal oxides with abundant active sites exposed like growing nanostructure arrays on conductive substrates and introduce porous or hollow structures. Zhang's group synthesized ultrathin δ - MoO_2 nanosheets on Ni foam by hydrothermal method [116]. The MoO_2 nanosheets were only two monolayer thick and exhibited an excellent HER activity in alkaline media due to abundant OVs and active sites. Other similar works were reported, such as porous MoO_2 nanosheets [117], porous WO_2 hexahedral networks [118], and NiCo_2O_4 hollow microcuboids [119].

In addition to synthesizing nanostructures, improving the intrinsic HER activity of metal oxides has been also well investigated. It is widely reported that creating OVs and heteroatom doping are promising strategies to enhance the unfavorable HER activity of pure metal oxides [120]. According to the first-principles calculations, the electrons near the defect are easier to be excited, thus improving the conductivity of the materials and optimizing the hydrogen adsorption energy [121]. For example, VO-enriched MoO_x and TiO_2 were applied as HER catalysts in an acidic solution [122, 123], while VO-enriched NiO and CoO can usually catalyze HER in alkaline media [124, 125]. It is worth noting that excessive OVs might reduce catalytic activity

due to structural instability and decreased electronic conductivity [126]. Therefore, it is important to adjust the OV concentration in catalysts to obtain the highest conductivity and HER activity.

The heteroatom doping can be divided into non-metal doping and metal doping. Non-metal doping is considered as an effective way to induce OVs in metal oxides. For instance, Zhang et al. reported that N-doped NiO could modulate the surface charge redistribution and induce OVs to facilitate the water dissociation, adsorption of H_{ad} , and desorption of OH_{ad} [127]. Other dopants were also reported, including P dopants in MoO_{3-x} nanosheets [128] and Co_3O_4 [129] and S dopants in CoO_x [130] and MoO_2 nanosheets [131]. Metal doping is another way to tune the electronic structure of metal oxides to optimize the hydrogen adsorption energy, which has also been widely engaged in binary metal oxides (Ni-doped Co_3O_4 nanosheets [132], $NiFe_2O_4$ [133], $ZnCo_2O_4$ [134], and $CuCo_2O_4$ [135]) and ternary metal oxides ($Ce-MnCo_2O_4$ [136], Mo-doped NiFe oxide nanowires [137], and Ni/Zn co-doped CoO nanorods [138]).

Metal (oxy)hydroxides are usually poor HER catalysts because of the unfavorable hydrogen adsorption energies. Considering that the metal (oxy)hydroxides are normally the active materials for OER and exhibit excellent water adsorption and dissociation properties, the metal (oxy)hydroxides can be coupled with other HER active materials to achieve excellent HER activity. Zhang et al. synthesized a three-dimensional (3D) hierarchical heterostructured NiFe layered double hydroxide (LDH) on NiCoP, which required a low overpotential of 120 mV for HER [139]. The interface between LDH and NiCoP increased the electrochemical surface area (ECSA) and optimized the reaction kinetics. Chen et al. prepared Ru-doped NiFe-LDH, which exhibited an ultralow overpotential of 29 mV in 1.0 M KOH [140]. The Ru dopants were beneficial in lowering the kinetic energy barrier of the Volmer step. Recently, other structures, such as NiCoP@NiMn LDH [141], NiCoP nanowires@NiCo LDH [142], CoSe/NiFe LDH [143], and CuO@CoFe LDH [144], were also reported to show good HER activities.

1.2.2 Oxygen Evolution Reaction

1.2.2.1 Mechanism

Compared with HER that involves two electrons, OER, a four-electron transfer reaction, is kinetically sluggish, making it the rate-limiting process of overall water splitting. Despite its importance, the mechanism of OER is not as well-studied as HER, mainly due to its complexity in different catalytic systems, as well as various reaction conditions.

In recent decades, several reaction mechanisms have been developed based on the results from different materials. Two of them are generally accepted: adsorbate evolution mechanism (AEM) and lattice oxygen mechanism (LOM), which are shown in Figure 1.9 [146]. It should be noted that the mechanism depends heavily on the reaction conditions and surface features of electrocatalysts, thus not fixed.

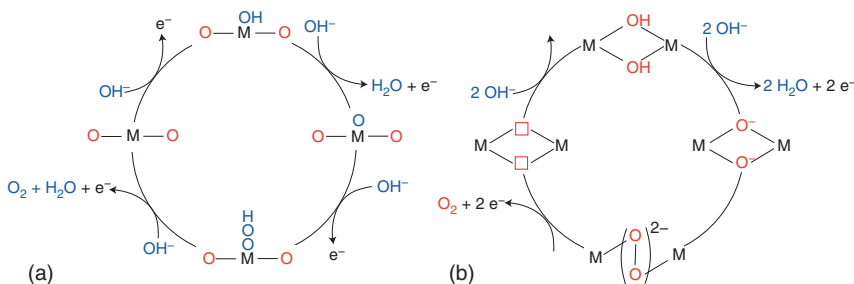
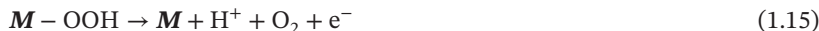
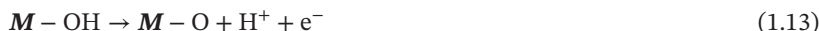


Figure 1.9 Mechanism of OER: (a) adsorbate evolution mechanism and (b) lattice oxygen mechanism. Source: Grimaud et al. [145]. Reproduced with permission of Springer Nature.

The AEM involves four concerted proton–electron transfer (CPET) processes occurring on the metal surface as follows:



After the adsorption of hydroxide anion (OH^-) on the active site \mathbf{M} (Eq. (1.12)), the adsorbed OH undergoes subsequent deprotonation to form O species (Eq. (1.13)), which can react with another OH^- to form $\mathbf{M}-\text{OOH}$ intermediate (Eq. (1.14)). Such intermediate is not stable and eventually releases O_2 and regenerates the active sites (Eq. (1.15)). The overall OER activity, therefore, is determined by all four steps. The ideal situation where all reactions occur at exactly 1.229 V (pH = 0) or 0.401 (pH = 14), the thermodynamic potential of OER at standard conditions, is almost impossible because the adsorption energy for the intermediates, from OH to O to OOH, is linearly correlated (scaling relation) (Figure 1.10a) [147]. For the binding energy of OOH and OH on catalytic sites, regardless of metals or metal oxide surfaces, both species involve a $\mathbf{M}-\text{O}$ single bond structure with a constant difference of Gibbs free energy ($\Delta G_{\text{OOH}} - \Delta G_{\text{OH}}$) of 3.2 ± 0.2 eV. For most catalytic systems, the reactions (1.13) and (1.14) are the RDS. Therefore, the free energy difference between O and OH bindings ($\Delta G_{\text{O}} - \Delta G_{\text{OH}}$) can be used as a universal descriptor to interpret and predict the OER activity of various materials [148].

Similar to the volcano-shaped relationship for HER (Figure 1.4), the $\Delta G_{\text{O}} - \Delta G_{\text{OH}}$ value also exhibits a volcano trend for various materials (Figure 1.10b). Regardless of the type of catalysts, OER only occurs when the species have neither too strong nor too weak adsorption strength. Thus, tuning the electrocatalyst surface for suitable adsorption energy to minimize the potential required for reactions (1.13) and (1.14) is the main target for rational OER catalyst design.

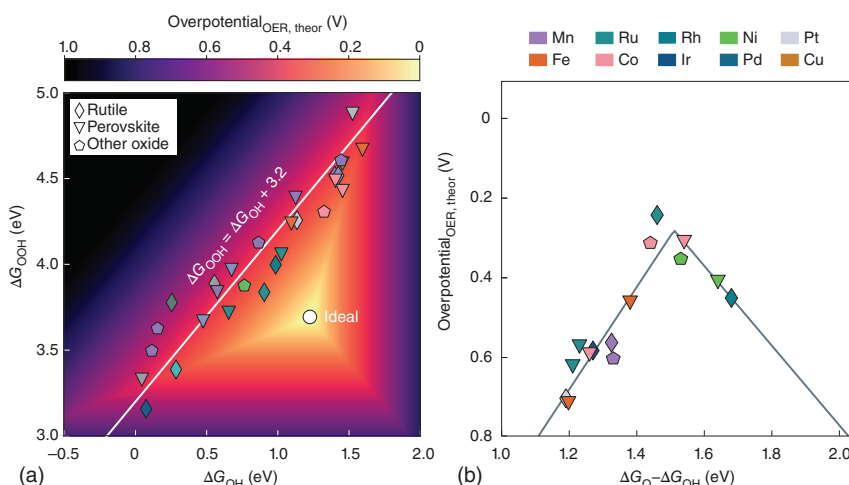


Figure 1.10 (a) Linear scaling relation of $\text{M}-\text{OOH}$ and $\text{M}-\text{OH}$ Gibbs free energy on a heat map of OER overpotential. Source: Man et al. [147]. Reproduced with permission of Springer Nature. (b) OER volcano plot for rutile, perovskite, and other metal oxides. Source: Montoya et al. [148]. Reproduced with permission of Wiley.

Another often referred OER mechanism is LOM. Different from AEM that only one metal site is considered, LOM engages two neighboring metal sites (Figure 1.9b). The two OH species on the metal sites firstly release proton to form $\text{M}-\text{O}-\text{M}$ species, followed by direct coupling to establish O—O bonding other than $\text{M}-\text{OOH}$ formation in AEM. The discharge of O_2 leaves two vacancies for two OH^- anions to adsorb. Since the LOM mechanism does not produce $\text{M}-\text{OOH}$ species, the scaling relation shown in Figure 1.10a does not exist.

Compared with AEM, the role of lattice oxygen in LOM still lacks a full understanding. In 2017, Grimaud et al. showed direct experimental evidence that the O_2 generated during OER on some highly active sites of perovskites were actually from the material lattice [149]. Further evidence indicated that the switching of reaction pathway from AEM to LOM was dependent on the metal–oxygen covalency. Moreover, some conventional materials, such as $\text{Co}_3(\text{PO}_4)_2$ [150] and IrO_2 [151], which was believed to follow AEM mechanism, have been proven to adopt LOM mechanism under some specific conditions.

The understanding of OER mechanism benefits and guides the rational design of OER catalysts. Based on AEM, reducing the $\Delta G_{\text{O}} - \Delta G_{\text{OH}}$ value is the key for high performance, and methods such as surface doping, vacancy creation, lattice strain engineering, and interfacial engineering have been widely adopted [146]. However, limited by the scaling relation of AEM, a minimal theoretical overpotential of 0.37 eV was predicted [152] while such limitation does not apply to LOM, allowing more freedom for materials discovery, such as bimetallic sites modulation to tune the metal–oxygen covalency.

Still, it is of great importance to point out that OER mechanism is currently under debate. Even for the most well-studied systems, such as IrO_2 , a recent study by

Nong et al. proposed a very different mechanism that the potential has no direct impact on the reaction coordination but affects the charge accumulation in the catalyst. As the amount of oxidative charge builds up, the activation free energy decreases linearly [153].

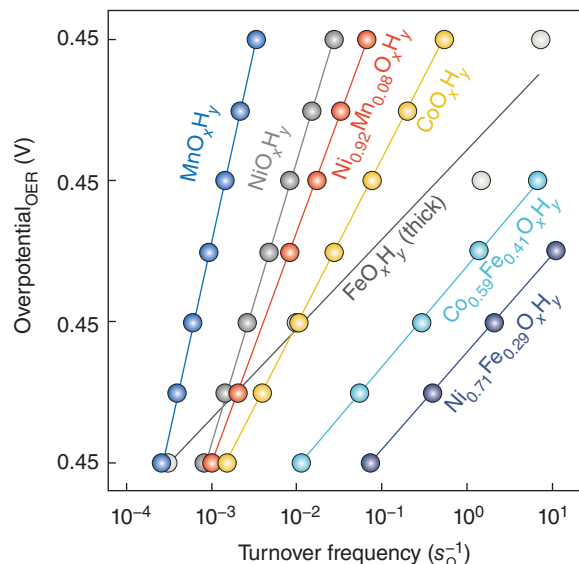
1.2.2.2 Metal Oxides/Hydroxides

Discussing or using metallic (M^0) nanoparticles for OER is not so meaningful since the oxidation of metal species generally occurs at a potential lower than OER requirement. Metal oxides and hydroxides are the most common forms of earth-abundant elements as OER electrocatalysts, and thousands of OER catalysts have been reported and proposed [154]. Burke et al. investigated the activity trend of a series of ultrathin metal oxides/hydroxides coated on Au electrode (Figure 1.11) and showed that bimetallic NiFeO_xH_y is the most promising system among the studied with an overpotential of 336 mV at 10 mA cm^{-2} and a Tafel slope of 30 mV dec^{-1} [155].

In the following contents, current systems showing significant potential for large-scale application and insights for fundamental understanding, such as doped Ni-/Co-based oxides/hydroxides, are introduced briefly.

Ni-Based Oxides/Hydroxides Ni-based oxides and hydroxides are the most popular catalysts so far, and they are the current commercial alkaline water electrolysis catalysts. NiO_x and Ni(OH)_2 are as active as noble metal-based ones (e.g. IrO_2) for OER: electrochemical deposited NiO_x shows an overpotential of 420 mV for 10 mA cm^{-2} in 1.0 M NaOH electrolyte (Figure 1.12) [157]. Reducing the size of catalysts can significantly improve the catalytic performance due to the enlarged surface area and enhanced conductivity: nano- Ni(OH)_2 (2.3 nm) and NiO_x (6 nm) can deliver

Figure 1.11 Experimental OER activity vs. turnover frequencies (TOF, O_2 generated per second per metal cation) of electrodeposited (oxy)hydroxides on Au microbalance electrodes. Source: Burke et al. [155]. Reproduced with permission of American Chemical Society.



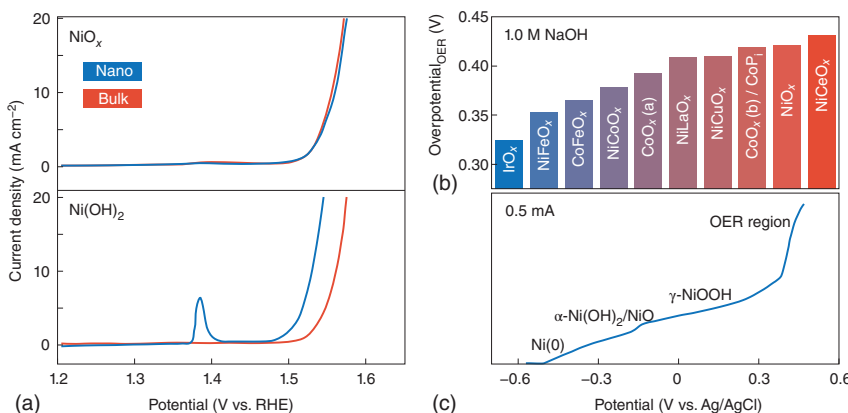


Figure 1.12 (a) Comparison of the OER activity of bulk NiO_x and Ni(OH)_2 with the nanostructured ones. Source: Stern and Hu [156]. Reproduced with permission of Royal Society of Chemistry. (b) Overview of the OER overpotentials (at 10 mA cm⁻²) of a few metal oxides in 1.0 M NaOH. Source: McCrory et al. [157]. Reproduced with permission of American Chemical Society. (c) Chronopotentiometry measurement of Ni nanoparticle oxidation at a low current of 0.5 mA. Source: Huang et al. [158]. Reproduced with permission of Wiley.

much lower overpotential of 300 and 330 mV under the same conditions, respectively (Figure 1.12a) [156]. During the potential-driven polarization, it is generally accepted that the Ni(II) species first convert to Ni(III) species, in the form of NiOOH (or NiO(OH)) (Figure 1.12c) [158, 159]. By directly engaging NiOOH for OER, higher activities were demonstrated, especially in non-extreme pH ranges, such as the neutral electrolyte. A recent work by Li et al. showed that nanosized NiOOH owns a high concentration of Ni cationic vacancy, providing a large number of active sites for Ni–OOH intermediate formation [160].

Recently, it was noticed that the iron impurities, even in the level of ppm, in the electrolyte and Ni-based oxide/hydroxide can significantly impact OER activity (Figure 1.11) [161, 162]. Most of the earlier studies of Ni-based OER catalysts were likely impacted by such impurity since iron is the most common impurity during Ni refine. Experimental evidence suggested that Fe atoms can gradually dope into the phase of formed $\gamma\text{-NiOOH}$ during polarization, promoting the phase transition to $\beta\text{-NiOOH}$. Such Fe doping can dramatically increase the electronic conductivity. It is also believed that Fe atoms exert a partial-charge-transfer activation effect on Ni atoms, resulting in high OER performance [163]. Recent DFT calculations showed that the formation energy of Ni–O can be reduced via Fe doping [164]. For Ni–Fe systems, an overpotential trend of Fe-doped $\beta\text{-NiOOH}$ (0.26 V) < NiFe_2O_4 (0.42 V) < $\beta\text{-NiOOH}$ (0.46 V) < Fe-doped $\gamma\text{-NiOOH}$ (0.48 V) < $\gamma\text{-NiOOH}$ (0.52 V) < Fe_3O_4 (0.70 V) was predicted by Li and Selloni [161]. Among other doped Ni-based oxides/hydroxides, such as Mo [165], W [166], and Co [167], the Fe–Ni system has shown by far the best efficiency. A guideline work for the surface doping on NiOOH (Figure 1.13) by Oscar Diaz-Morales et al. shows that, when Mn, Fe, Co, Cu, and Zn are engaged on the surface of NiOOH, the overpotential of Ni sites increases slightly while Cr causes decrement. However, the Fe and Mn sites themselves are much active for OER than the Ni sites [168].

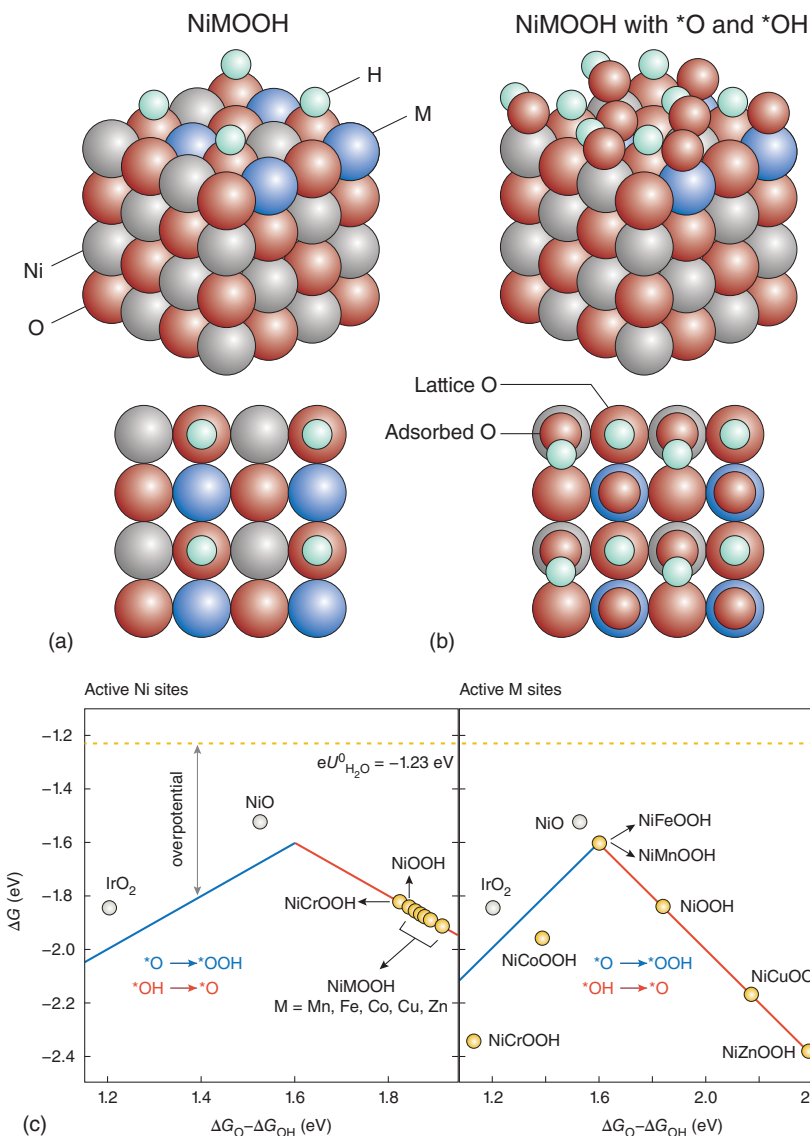


Figure 1.13 Perspective and top views of M-doped NiOOH (001) surface: (a) clear and (b) with *O and *OH adsorbed on M and Ni, respectively. (c) OER volcano plots of M-doped NiOOH with Ni sites (left) and M sites (right) as the active sites. Blue and red lines indicate the potential limiting steps: the blue part is limited by the transformation of *O to *OOH , and the red part is limited by the *OH to *O transition. M = Cr, Mn, Fe, Co, Ni, Cu, and Zn. Source: Diaz-Morales et al. [168]. Reproduced with permission of American Chemical Society.

Further surface engineering of Fe-doped Ni oxides/hydroxides provides extra tunability of OER activity. For example, Fe and V were co-doped to Ni oxide to modulate the local coordination sites of Fe/V/Ni cations. The V sites, surprisingly, showed near-ideal binding energy for OER intermediates and the lowest overpotential compared with nearby Ni and Fe sites [169]. Similar trimetallic systems, such as MoFeNi oxides/hydroxides [165], also showed superior OER performance than their mono/bimetallic siblings. Another extreme case is NiFeCoCeO_x catalytic system where Ni, Fe, and Co are the active sites [170]. Nearly all doped systems attributed the high activity to the synergistic effect between metal cations, increasing the interaction strength of active sites with OH species. Other non-metallic doping examples are also proven effective [171].

Doping strategy focuses on tuning the electronic properties of metal sites. Another commonly applied method is altering the shape to expose more active sites. One of the most efficient ways to achieve high surface area is to increase the porosity of materials. For instance, Fe-doped β -Ni(OH)₂ porous structure showed a low overpotential of 218 mV in alkaline media [172]. Making the metal hydroxide into 2D forms to enlarge the number of facial atoms is also a popular approach. Luan et al. studied the morphologic effect of Ni(OH)₂ in OER using layer-stacked bud-like, flower-like, petallike, and ultralarge sheetlike Ni(OH)₂. The petallike Ni(OH)₂ showed the best performance with an overpotential of 260 mV and Tafel slope of 78.6 mV dec⁻¹ among all shapes. Although the sheetlike Ni(OH)₂ owns a high diffusion rate, the petal-like Ni(OH)₂ with small particle size offers more boundary sites for OER [173].

In addition to modifying the electronic and structural properties of Ni-based oxides/hydroxides, engineering the electrocatalyst support for better electronic transfer is equally crucial since most metal oxides/hydroxides are semiconducting. Supports that can improve the interfacial resistance between catalyst and electrode have been explored, such as CNTs [174], graphene [175], and carbon nitride [176]. The support, on the other hand, offers another dimension for the electronic tuning of Ni-based materials. In the case of C₃N₄, the formation of Ni—N bonding between the NiO and C—N units can lower the Gibbs free energy for OER intermediate adsorption, improve the charge transfer rate, and promote mass diffusion rate at the same time [176].

Co-Based Oxides/Hydroxides Cobalt oxides are highly active OER electrocatalysts, which can offer comparable performance to Ni-based ones. Regardless of the valent states of the catalysts before reaction, such as metallic Co(0) nanoparticles, Co(II) oxide, and Co(III) oxides, it is commonly accepted that the oxidation of Co(III) to Co(IV) species (CoO₂) is the precatalytic conversion before O₂ discharge. However, the full details of OER on Co oxides and hydroxides are still under debate [177]. *In situ* (or *operando*) methods are heavily relied on for understanding the reaction mechanism of Co-based materials. Favaro et al. pointed out that full conversion of Co(OH)₂ and partial conversion of Co₃O₄ to CoOOH is inevitable, starting at a potential lower than that of thermodynamic OER. Such CoOOH species, as suggested by the *operando* photoelectron spectra, are responsible for generating highly active Co(IV) center for OER [177]. Bergmann et al. added that Co-based

catalytic systems, independent of their initial Co or coordination states, transform into a universal structure of HO-bridged Co(II)/Co(III) ion clusters, where the reducible Co(III)-O sites are the active sites for general OER activity [178]. However, Moysiadou et al. recently argued that, based on their *operando* results, the RDS of OER on amorphous CoOOH is the release of O₂ from the superoxide intermediate produced during the Co(III) to Co(IV) oxidation [179]. Based on such findings, any OER performance differences of electrocatalysts based on different valent states of Co can be addressed by the surface area of *in situ* generated Co(III)/Co(IV), as confirmed experimentally by Chou et al. using Co, CoO, and Co₃O₄ nanoparticles with similar surface areas [180].

Currently, the most studied materials among all are spinel cobalt oxide (Co₃O₄), cobaltite (MCo₂O₄, M = Ni, Cu, Mn, etc.), cobalt hydroxide (Co(OH)₂), and cobalt oxyhydroxide (CoOOH) [181]. In general, two fundamental issues of the Co-based electrocatalysts are targeted: active site engineering and conductivity improvement.

Active site engineering includes increasing the total population of Co sites and boosting the activity of Co sites. For the former aspect, typical methods include decreasing particle size and controlling the morphology and crystalline phases. For example, Sidhureddy et al. compared the OER performance of shape-controlled Co₃O₄, from one-dimensional (1D) nanorod to 3D nanocube, and reported that the 2D nanosheets showed the best performance due to its high surface area and abundant oxygen defects [182]. For the latter aspect, tuning the activity Co sites requires electronic interaction, and the most frequently visited method is metal doping. The involvement of another (or more) cation(s) in Co oxides/hydroxides often leads to a direct impact of the Co(IV) formation and phase conversion, as well as the creation of oxygen vacancy. Fe [183, 184], Cu [185], and Ni [186] are the most popular choices while cases using Mn [187], Ca [188], and Ti [189] are also reported. Direct doping on CoOOH is also a popular choice [190]. Recently, doping of non-metallic elements, such as S [191] and Cl [192], is gaining attention as an effective way of forming direct bonding between Co and the anions, unlike the bimetallic -Co-O-M- formation using metal doping. Chen et al. introduced fluorine anions (F⁻) on the surface of CoOOH, creating a more hydrophilic surface of electrocatalysts to benefit the OH⁻ adsorption [193].

Extensive doping leads to the formation of bimetallic (or trimetallic) oxides/hydroxides. The most promising systems include NiCoO_xH_y [194] and FeCoO_xH_y [195, 196], which commonly deliver much lower overpotential than the monometallic compounds. For instance, FeCoO_xH_y 2D nanosheets developed by Zhuang et al. exhibited a high current density of 54.9 A g⁻¹ with an overpotential of 350 mV [195]. The low Tafel slope of 36.8 mV dec⁻¹ makes it one of the best electrocatalytic systems reported so far. Such work is a typical example of combining both morphologic and electronic engineering for OER catalyst.

Metal doping can also significantly improve the conductivity of metal oxides/hydroxides due to the creation of vacancies in the semiconducting structure. Another method to reduce the charge transfer resistance is the support engineering. Similar to previously mentioned Ni-based systems, CNTs [197] and functionalized carbon supports [198] are generally engaged.

Fe-Based Oxides/Hydroxides Iron is the most abundant transition metal element on earth crust and is much cheaper than cobalt and nickel. However, in their bulk forms, such as FeO and Fe(OH)₂, the electronic conductivities are generally low [199], limiting the application of most Fe-based oxides/hydroxides for OER electrocatalysis.

Comparing with Ni and Co, the fundamental studies on Fe oxides/hydroxides are not broad. The doping of Fe in Ni/Co-based materials is proven effective and discussed earlier in this section. Lyons and Brandon proposed the redox couple of Fe(III)/Fe(VI) to accompany the OER on Fe oxyhydroxide electrode [200]. Systematic work by Boettcher's group showed that the OER behavior of FeOOH depends on the applied overpotential. At a low overpotential, the activity of FeOOH is impacted by the supporting electrode (Au/AuO_x in their study) where the interfacial Fe cations are active. At a high overpotential, on the other hand, the electrical conductivity of FeOOH increases, benefitting the OER process [199].

Current research focus, therefore, is to improve the conductivity of Fe-based oxides/hydroxides. Once again, metal doping and catalyst support engineering are preferred pathway. Some state-of-the-art systems include Co-doped FeOOH [201], Cu-doped FeOOH [202], Se-doped FeOOH [203], Ti-doped FeOOH [204], and a series of transition metal-doped Fe₂O₃ [205] and Fe₃O₄ [206].

Other Oxides/Hydroxides Studies on other earth-abundant metal element-based oxides and hydroxides, including Cu, Ti, Mn, Mo, and V, are not as booming as Ni/Co/Fe-based ones due to their low activities. A brief introduction is given below with the selected cases:

Cu based: Liu et al. demonstrated that CuO electrocatalyst could perform OER at a rate of 1.0 mA cm⁻² with an overpotential of 430 mV. Although outperformed by Ni/Co/Fe, it is one of the best results achieved for Cu-based system [207]. Making the bulk nanoparticle into 2D shape benefits the mass transfer and surface enlargement, as suggested by the catalytic results of 2D CuO electrocatalyst that delivered an overpotential of 350 mV at 10 mA cm⁻² in 1.0 M KOH [208]. Metal doping improves the catalytic performance significantly: Co-doped CuO with Co atomic ratio of c. 10% recorded an overpotential of 330 mV to achieve 100 mA cm⁻² [209]. An example of morphologic effect was reported by Huan et al. using dendritic nanostructured CuO, which demonstrated an even lower overpotential of 290 mV at 10 mA cm⁻² [210].

Ti based: TiO₂ is well known for its photo(electro)catalytic activity, which is beyond our scope in this chapter. Pure TiO₂ has low electrical conductivity and is predicted to have a very high overpotential for OER [211]. However, theoretical calculations suggested that earth-abundant metal-doped (Cr, Mo, and Mn) TiO₂ could share OER activity similar to RuO₂ [212].

Mn based: Mn_xO_y family (e.g. MnO₂, Mn₂O₃, and Mn₃O₄) is considered as a promising OER catalyst due to its stability under extreme pH conditions (especially in acidic conditions where Ni/Co/Fe-based electrocatalysts are not stable) and abundance [213]. Nocera's group has focused on understanding the OER mechanism

on Mn_xO_y [214, 215] and showed that the stabilization of Mn(III) species is the key to promote O_2 formation [216]. The best performance so far was obtained using Mn_2O_3 nanotube arrays coated on conductive Ni foam, which showed an overpotential of 270 mV at 10 mA cm⁻² and a Tafel slope of 85 mV dec⁻¹ [217]. Current studies focus on the morphologic tuning of Mn_xO_y for better conductivity. For example, using sub-10 nm MnO nanocrystals can facilitate the generation of surface Mn(III) species during polarization for improved OER [218]. Still, the major challenge lies in the understanding of Mn-based catalytic system and developing synthesis methods to achieve different morphology.

Mo based: The application of pure Mo oxides/hydroxides for electrochemical OER is rarely reported. One recent literature showed that, regardless of morphology, MoO_3 has a much higher overpotential than most other metal oxides/hydroxides discussed. Even with the help of graphene to reduce the resistance, an overpotential of c. 540 mV was required to deliver merely 0.12 mA cm⁻² [219]. Currently, Mo is used only as doping elements to modify the properties of hosting materials, such as $\text{Ni}(\text{OH})_2$ and $\text{Co}(\text{OH})_2$.

V based: V-based oxides/hydroxides are widely used for electrochemical applications. The valence of V ranges from V(II) to V(III) to V(IV) to V(V) in vanadium oxides, offering various oxygen coordination environments for OER. V cations themselves, however, are not active for OER. The most frequently referred OER catalytic systems are MVO_xH_y (M = Co, Ni) [220, 221]. For example, Jiang et al. developed a $\text{Ni}_3\text{Fe}_{1-x}\text{V}_x$ hydroxide material, in which the V sites outperform Ni and Fe sites for OER due to the synergistic electronic effect [169].

1.2.2.3 Metal (Mn^+) Single-Atom Catalysts

Similar to the original intention of HER SACs, the development of OER SACs initially focused on lowering the loading of noble metals (Ru and Ir) and gradually expanded to earth-abundant metals [222]. For both HER and OER, the study of SACs shares the same challenge of preparing stable and efficient SACs, making the engineering of catalyst support a major topic [223]. Especially, the understanding of reaction mechanism on OER SACs is much more complicated than HER, given the limited technologies with atomic resolution and more complex OER pathway.

Currently, Fe, Ni, and Co SACs are among the most reported OER electrocatalysts. Chen et al. developed a Fe SAC with abundant Fe atoms decorated on N- and S-enriched carbon layer, which exhibited an overpotential of 370 mV at 10 mA cm⁻² and Tafel slope of 82 mV dec⁻¹. The authors argued that the Fe 3d-electrons are affected by the neighboring N and S atoms, resulting in largely improved electrical conductivity [224]. Zheng et al. demonstrated a series of $\text{M}-\text{C}_3\text{N}_4$ catalyst (M = Fe, Co, Ni) of OER activity, and $\text{Co}-\text{C}_3\text{N}_4$ could deliver similar activities with noble metal-based ones in alkaline media. They further identified that the $\text{M}-\text{OOH}$ formation governs the reaction rate, and the hosting N-rich environment for metal atoms is the key to stabilize isolated metal atoms. As the applied potential increases, the N-coordinated Co atoms are oxidized to Co^{3+} and higher states to catalyze OER [225]. Other SACs, beyond Fe, Ni, and Co, are rarely reported.

The coordinating atoms interacting with the metal sites define the catalytic performance of SACs. Other than N atoms, S [226] and O [227] coordinating atoms are also investigated. In some case, the coordination via S or O atoms shows more functionality in OER than electronically affecting the metal sites. For example, Huang and coworkers identified that the C atoms of a Ni-N₄-C₄ SAC could act as active sites for a dual reaction pathway OER [228].

Involving two or more metal atoms for SAC design is a proven strategy for HER, which allows fine-tuning of the activity of selected sites [229]. The same method also works for OER SACs. A Co-Fe double-atom electrocatalyst was prepared by *in situ* electrochemical treatment of Co SACs by Bai et al., and the Co-Fe dimeric unit was found to act as the active site [230]. Other combinations include Co-Mo (N-Co-Mo supported by graphene nanoflake-CNT composite) [231], Co-Ni (Co-Ni sites embedded in N-doped hollow carbon nanocubes) [232], and Fe-Ni (Fe-Ni in N-doped carbon hollow spheres) [233].

Overall, OER SACs are promising candidates for both high-efficient water splitting and theoretical understanding of the OER mechanism. Different combinations and various support choices make the study of SACs one of the fastest developing topics in both electrochemistry and energy-related catalysis. Yet, the durability of SACs should be proven before claiming any superiority over conventional materials. In this regard, the results from *in situ* techniques that can monitor the isolated active sites are always preferred for performance interpretation.

1.2.2.4 Metal Chalcogenides/Nitrides/Phosphides and Others

Materials other than typical metal and metal oxides are often proposed for OER, including metal chalcogenide (MX₂, M = Ti, Mo, or W, X = S, Se, or Te) [234], metal nitrides (M_xN, M = Co, Ni, Fe, etc.) [235], and metal phosphides (M_xP, M = Co, Ni, Fe, etc.) [236]. Many OER catalysts have reported even higher activity than commercial noble metal-based ones, as well as outstanding stability for hours. As discussed in the HER section (Sections 1.2.1.4–1.2.1.6), these materials are also active catalysts for HER. Based on their performances in both HER and OER, they are frequently claimed “bifunctional” despite being neither necessary nor efficient for real devices where the HER and OER are performed separately (Figure 1.1). However, based on the mechanism for OER, the establishment of metal–oxygen bonding is essential for **M**–OH formation. As pointed out by Song Jin [237], metal sulfides, as well as metal nitrides and phosphides, are thermodynamically less stable than metal oxides when subjected to external potential. Therefore, the formation of metal oxides/hydroxides is inevitable for all metal chalcogenides, metal nitrides, and metal phosphides as soon as they are placed in the electrolyte of extreme pH. Arguably, the surface metal oxides/hydroxides are the real OER catalysts, while the initial metal compounds are the precatalysts [238] (materials that produce real catalysts during the electrochemical process). Such opinion is confirmed by many literatures. For example, Ni₂P, one of the earliest metal phosphide OER electrocatalysts, generates a shell of NiO_x during OER process, explaining its ability to produce O₂ [239]. The real OER catalyst should be expressed, at least, as NiO_x/Ni₂P, other than just Ni₂P. Similarly, a report by Chen et al. on using metallic

Co_4N porous nanowire arrays for OER also acknowledged the existence of a CoO_x layer formed during the electrochemical test [240]. Due to the known high activity of CoO_x , it is unclear whether Co_4N contributes to OER activity or not.

Nevertheless, experimental results also proved that the coexisting M–S/N/P structures can affect the OER activity of outer metal oxides/hydroxides. Xu et al. studied the trend in OER activity in metal phosphides and revealed the activity order of $\text{FeP} < \text{NiP} < \text{CoP} < \text{FeNiP} < \text{FeCoP} < \text{CoNiP} < \text{FeCoNiP}$, which also agrees with the electronegativity of metal sites [241]. Although the surface is converted to metal oxides/hydroxides, the sublayer coordination environments still affect the OER sites.

Since the concept of precatalyst is now generally accepted in the research community, the rational design and understanding of metal chalcogenides/nitrides/phosphides in OER conditions require more carefully designed experiments and *in situ* techniques to uncover the proper reaction mechanism [242].

Other emerging materials, such as metal–organic frameworks, were also reported suitable for OER but shared the same problems discussed above. For example, Ghoshal et al. suggested ZIF-67 (zeolitic imidazolate framework with Co sites) as a highly active OER catalyst [243]. Later, by using *in situ* spectroelectrochemistry, Zheng et al. found that the structure of ZIF-67 is not stable during electrochemical studies and $\alpha/\beta\text{-Co(OH)}_2$ are the real active species for OER, not the Co sites (Figure 1.14) [244]. Moreover, even without a redox reaction occurring on the Co sites, the sweeping potential can sabotage the weak Co–N coordination sites within a few seconds.

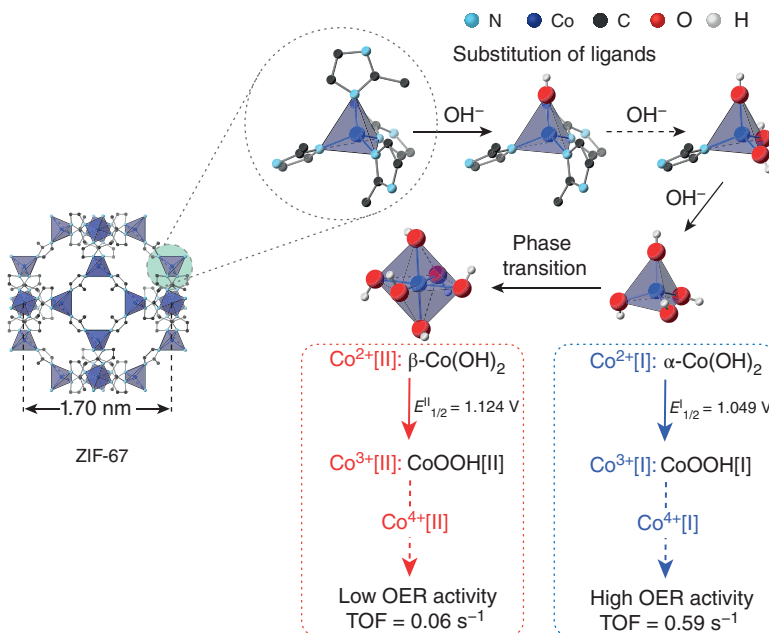


Figure 1.14 Precatalytic conversion of ZIF-67 to $\alpha/\beta\text{-Co(OH)}_2$ and the experimental OER activity of both Co(OH)_2 . Source: Zheng et al. [244]. Reproduced with permission of American Chemical Society.

1.3 Computer-Assisted Materials Discovery

The prosperous development of material science in the last decade has led to the explosive increment in numbers and categories of materials for water splitting. Apparently, it is impossible for any research group in the world to prepare all the materials and benchmark them under the identical condition as before. For example, the bimetallic/trimetallic (or even more) doping on metal oxides/hydroxides OER catalyst can have a doping level from ppm to 100% surface coverage. Besides, metal sites can be doped on different crystalline facets with different ratios. Such factors in practical experimental conditions provide nearly infinite combinations for potentially high OER activity. Experimentally, it can be challenging to prepare the material and confirm the structure–activity relationship.

Computer-assisted materials discovery, including DFT prediction and machine learning, are the future for material design and discovery of electrocatalysts, including HER and OER [245, 246]. Using DFT calculations for understanding the reaction pathway has been a standard technology in the last couple of decades [247]. Meanwhile, the high-throughput screening of water splitting electrocatalysts also has gained wide attention: not only the activity but also stability can be readily predicted. In 2006, Greeley et al. presented a DFT-based screening scheme for HER electrocatalyst involving over 700 binary surface alloys (Figure 1.15), where the superiority of BiPt over Pt was predicted and experimentally confirmed [248]. Later, Björketun et al. exploited a collection of theoretical and experimental databases and

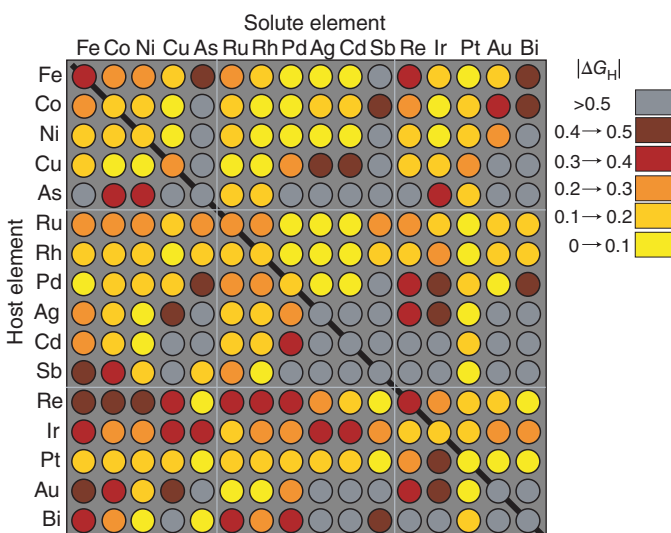


Figure 1.15 Computational high-throughput screening of HER catalyst for ΔG_H on 256 combinations. Source: Greeley et al. [248]. Reproduced with permission of Springer Nature.

found that a binary “substrate–overlayer” of Cu–W is HER active, confirmed by their experiments [249]. Similar predictions were also made for OER catalyst design. For instance, a family of Ni–Fe–Co–Ce oxides was screened by Haber et al., and the compositions of $\text{Ni}_{0.5}\text{Fe}_{0.3}\text{Co}_{0.17}\text{Ce}_{0.03}\text{O}_x$ and $\text{Ni}_{0.3}\text{Fe}_{0.07}\text{Co}_{0.2}\text{Ce}_{0.43}\text{O}_x$ were proposed with excellent OER performance and stability [250]. Obviously, it would take years of material synthesis and testing to confirm such a combination without such prediction. Even for systems that are not available due to experimental difficulty, their potential activity can be studied conveniently such as $\text{MoTe}_2/\text{WTe}_2$ layered material with an interlayer rotation angle of 300° and was predicted to have an overpotential of 30 mV for HER and 170 mV for OER [251].

Current experimental techniques do not limit the computer-assisted materials discovery, but the calculation power does. The rapid advances in computer science have significantly shortened the calculation time in complex systems and improved accuracy. For researchers not familiar with computational chemistry, a few public/open calculation projects/databases are currently available for preliminary material screening, calculation, and property prediction, which mainly include the following:

Open Catalyst Project: <https://opencatalystproject.org>

Materials Cloud: <https://www.materialscloud.org>

The Materials Project: <https://materialsproject.org>

Novel Materials Discovery (NOMAD): <https://nomad-lab.eu>

Automatic-Flow for Materials Discovery (AFLOW): <http://aflowlib.org>

The Open Quantum Materials Database (OQMD): <http://oqmd.org>

1.4 Challenge and Outlook

Hydrogen production by electrochemical water splitting is one of the most promising and feasible ways to realize the large-scale application of hydrogen fuel but currently has few challenges.

1.4.1 Reliability Comparison Between Results

Numerous publications on HER and OER electrocatalysts that appear every day make it increasingly challenging to benchmark the electrocatalysts among various research groups, mainly due to the difference in reaction conditions (scan rate, electrolyte, electrocatalyst pretreatment, electrocatalyst supporting electrode), experimental setups (electrolyte, reference/counter electrode, potential/current sequence), data treatment (current density calculation), and so on.

To confront such problems in the electrochemical community, various guideline papers have been published recently trying to address the experimental issues.

The most important ones are introduced here to benefit the junior researchers to correctly evaluate the HER/OER activity of materials:

For general water electrolyzer: Essential parameters required for material characterization and water splitting performance evaluation [252].

For heterogeneous electrocatalyst: Benchmarking catalyst, electrochemical surface area calculation, and counter electrode selection [253, 254].

For HER/OER electrocatalyst: Electrochemical cell, selection of counter electrode, and contamination of working electrodes [255], essential parameters and ways to report [256]; and problems associated with using conductive foam as supporting electrode [257].

1.4.2 Gap Between Industrial and Laboratorial Research

Currently, many electrocatalytic systems in literature have demonstrated excellent HER and OER activities that outperform the costly commercial noble metal-based electrocatalysts. Yet, they are not quickly commercialized as expected. One of the major issues is the different operating conditions between industrial and laboratorial researches. Most published materials are tested under standard laboratorial conditions: small scale, electrolyte of 0.5 M H_2SO_4 /1.0 M KOH, room temperature, low current, small working area, etc. Conventional industrial water electrolysis, however, operates at higher temperature ($>60^\circ\text{C}$) with extreme pH (30% KOH electrolyte for alkaline water electrolysis). Much higher durability is also required since it is impractical to change the electrocatalyst every a few hours. Most importantly, the “novel nanomaterials,” despite having low cost of ingredients, are difficult and expensive to be prepared in large quantities. Fancy and fragile nanostructures, although sometimes show attractive performance, are not actually cheaper than the noble metal-based ones due to their high manufacturing cost and poor stability under industrial conditions.

Currently, PEM process for water electrolysis has been proven more efficient than alkaline water splitting, but most earth-abundant metal-based HER/OER catalysts are not suitable for application under acidic conditions, especially at high temperature. The development of such catalytic systems is urgently required for commercial PEM devices.

1.4.3 Outlook

Today, we are witnessing the key transition of the thousand-year-old carbon-based energy economy to the sustainable hydrogen-based energy economy. Due to the increasing environmental concerns, many countries and organizations, including China, European Union, Japan, South Korea, and United Kingdom, have committed in law to achieve carbon neutrality between 2050 and 2060. Compared with the last century, remarkable progresses have been achieved in the past few years on water

splitting, and more commercial HER/OER electrocatalysts are expected within next 10 years. The rational design of durable and efficient HER/OER electrocatalysts based on earth-abundant metal elements will be the key topic in energy-related electrochemistry.

References

- 1 IRENA (2019). *Hydrogen: A Renewable Energy Perspective*. Abu Dhabi.
- 2 Levin, D.B. and Chahine, R. (2010). *Int. J. Hydrogen Energy* 35: 4962–4969.
- 3 Valente, A., Iribarren, D., and Dufour, J. (2020). *Sci. Total Environ.* 728: 138212.
- 4 Shinagawa, T. and Takanabe, K. (2017). *ChemSusChem* 10: 1318–1336.
- 5 Sun, X., Xu, K., Fleischer, C. et al. (2018). *Catalysts* 8: 657–697.
- 6 Rumble, J. (2020). *CRC Handbook of Chemistry and Physics*, 101e. CRC Press.
- 7 Lasia, A. (2019). *Int. J. Hydrogen Energy* 44: 19484–19518.
- 8 Trasatti, S. (1972). *J. Electroanal. Chem. Interfacial Electrochem.* 39: 163–184.
- 9 Skúlason, E., Tripkovic, V., Björketun, M.E. et al. (2010). *J. Phys. Chem. C* 114: 18182–18197.
- 10 Rojas, M., Fan, C.L., Miao, H.J., and Piron, D.L. (1992). *J. Appl. Electrochem.* 22: 1135–1141.
- 11 Behzadian, B., Piron, D., Fan, C., and Lessard, J. (1991). *Int. J. Hydrogen Energy* 16: 791–796.
- 12 Liu, L. and Corma, A. (2020). *Nat. Rev. Mater.* 6: 244–263.
- 13 Ouyang, G., Wang, C.X., and Yang, G.W. (2009). *Chem. Rev.* 109: 4221–4247.
- 14 Mayrhofer, K.J., Blizanac, B.B., Arenz, M. et al. (2005). *J. Phys. Chem. B* 109: 14433–14440.
- 15 Fei, H., Yang, Y., Peng, Z. et al. (2015). *ACS Appl. Mater. Interfaces* 7: 8083–8087.
- 16 Yu, H.Z., Wang, Y., Ying, J. et al. (2019). *ACS Appl. Mater. Interfaces* 11: 27641–27647.
- 17 Chen, Z., Wu, R., Liu, Y. et al. (2018). *Adv. Mater.* 30: e1802011.
- 18 Devi, B., Koner, R.R., and Halder, A. (2018). *ACS Sustainable Chem. Eng.* 7: 2187–2199.
- 19 Yan, X., Gu, M., Wang, Y. et al. (2020). *Nano Res.* 13: 975–982.
- 20 Gong, Y., Wang, L., Xiong, H. et al. (2019). *J. Mater. Chem. A* 7: 13671–13678.
- 21 Yang, L., Zhou, W., Jia, J. et al. (2017). *Carbon* 122: 710–717.
- 22 Du, J., Wang, L., Bai, L. et al. (2018). *ACS Sustainable Chem. Eng.* 6: 10335–10343.
- 23 Wang, L., Li, Y., Xia, M. et al. (2017). *J. Power Sources* 347: 220–228.
- 24 Tavakkoli, M., Kallio, T., Reynaud, O. et al. (2015). *Angew. Chem. Int. Ed.* 54: 4535–4538.
- 25 Wang, J., Wang, G., Miao, S. et al. (2014). *Faraday Discuss.* 176: 135–151.

26 Ahmed, J., Trinh, P., Mugweru, A.M., and Ganguli, A.K. (2011). *Solid State Sci.* 13: 855–861.

27 Lu, Q., Hutchings, G.S., Yu, W. et al. (2015). *Nat. Commun.* 6: 6567.

28 Kuang, M., Wang, Q., Han, P., and Zheng, G. (2017). *Adv. Energy Mater.* 7: 1700193–1700200.

29 Ahsan, M.A., Puente Santiago, A.R., Hong, Y. et al. (2020). *J. Am. Chem. Soc.* 142: 14688–14701.

30 Wang, T., Guo, Y., Zhou, Z. et al. (2016). *ACS Nano* 10: 10397–10403.

31 Ahmed, J., Kumar, B., Mugweru, A.M. et al. (2010). *J. Phys. Chem. C* 114: 18779–18784.

32 Khani, H., Grundish, N.S., Wipf, D.O., and Goodenough, J.B. (2019). *Adv. Energy Mater.* 10: 1903215–1903224.

33 Qiao, B., Wang, A., Yang, X. et al. (2011). *Nat. Chem.* 3: 634–641.

34 Hunt, S.T., Milina, M., Wang, Z., and Román-Leshkov, Y. (2016). *Energy Environ. Sci.* 9: 3290–3301.

35 Fei, H., Dong, J., Arellano-Jimenez, M.J. et al. (2015). *Nat. Commun.* 6: 8668.

36 Xue, Y., Huang, B., Yi, Y. et al. (2018). *Nat. Commun.* 9: 1460.

37 Qiu, H.J., Ito, Y., Cong, W. et al. (2015). *Angew. Chem. Int. Ed.* 54: 14031–14035.

38 Chen, W., Pei, J., He, C.-T. et al. (2017). *Angew. Chem. Int. Ed.* 129: 16302–16306.

39 Chen, W., Pei, J., He, C.T. et al. (2018). *Adv. Mater.* 30: e1800396.

40 Cao, L., Luo, Q., Liu, W. et al. (2018). *Nat. Catal.* 2: 134–141.

41 Wang, L., Liu, X., Cao, L. et al. (2020). *J. Phys. Chem. Lett.* 11: 6691–6696.

42 Chen, W., Pei, J., He, C.T. et al. (2017). *Angew. Chem. Int. Ed.* 56: 16086–16090.

43 Yang, Y., Qian, Y., Li, H. et al. (2020). *Sci. Adv.* 6: eaba6586.

44 Zhang, Q. and Guan, J. (2020). *Adv. Funct. Mater.* 30: 2000768–2000820.

45 Gutić, S.J., Dobrota, A.S., Fako, E. et al. (2020). *Catalysts* 10: 290–327.

46 Liu, H., Peng, X., and Liu, X. (2018). *ChemElectroChem* 5: 2963–2974.

47 Pu, Z.H., Amiinu, I.S., Cheng, R.L. et al. (2020). *Nano-Micro Lett.* 12: 21–49.

48 Li, X., Bi, W., Chen, M. et al. (2017). *J. Am. Chem. Soc.* 139: 14889–14892.

49 Gao, G., Bottle, S., and Du, A. (2018). *Catal. Sci. Technol.* 8: 996–1001.

50 Fan, L., Liu, P.F., Yan, X. et al. (2016). *Nat. Commun.* 7: 10667.

51 He, T., Zhang, C., and Du, A. (2019). *Chem. Eng. Sci.* 194: 58–63.

52 Zhang, Y., Li, W., Lu, L. et al. (2018). *Electrochim. Acta* 265: 497–506.

53 Cao, Y., Chen, S., Luo, Q. et al. (2017). *Angew. Chem. Int. Ed.* 56: 12191–12196.

54 Ling, C., Shi, L., Ouyang, Y. et al. (2017). *Nano Lett.* 17: 5133–5139.

55 Sredojević, D.N., Belić, M.R., and Šljivančanin, Ž. (2020). *J. Phys. Chem. C* 124: 16860–16867.

56 Weng, C.C., Ren, J.T., and Yuan, Z.Y. (2020). *ChemSusChem* 13: 3357–3375.

57 Li, H., Lu, S., Sun, J. et al. (2018). *Chemistry* 24: 11748–11754.

58 Xiao, P., Sk, M.A., Thia, L. et al. (2014). *Energy Environ. Sci.* 7: 2624–2629.

59 Kibsgaard, J., Tsai, C., Chan, K. et al. (2015). *Energy Environ. Sci.* 8: 3022–3029.

60 Du, H., Kong, R.M., Guo, X. et al. (2018). *Nanoscale* 10: 21617–21624.

61 Guan, C., Xiao, W., Wu, H. et al. (2018). *Nano Energy* 48: 73–80.

62 Wang, X., Zhou, H., Zhang, D. et al. (2018). *J. Power Sources* 387: 1–8.

63 Man, H.-W., Tsang, C.-S., Li, M.M.-J. et al. (2019). *Appl. Catal., B*. 242: 186–193.

64 Liu, T., Liu, D., Qu, F. et al. (2017). *Adv. Energy Mater.* 7: 1700020.

65 Zhou, Q., Shen, Z., Zhu, C. et al. (2018). *Adv. Mater.* 30: 1800140.

66 Chang, J., Li, K., Wu, Z. et al. (2018). *ACS Appl. Mater. Interfaces* 10: 26303–26311.

67 Liang, K., Pakhira, S., Yang, Z. et al. (2019). *ACS Catal.* 9: 651–659.

68 Zhang, T., Yang, K., Wang, C. et al. (2018). *Adv. Energy Mater.* 8: 1801690.

69 Wang, Z., Du, H., Liu, Z. et al. (2018). *Nanoscale* 10: 2213–2217.

70 Zhang, X., Zhu, S., Xia, L. et al. (2018). *Chem. Commun.* 54: 1201–1204.

71 Wu, Z., Wang, J., Xia, K. et al. (2018). *J. Mater. Chem. A* 6: 616–622.

72 Wang, A.-L., Lin, J., Xu, H. et al. (2016). *J. Mater. Chem. A* 4: 16992–16999.

73 Luo, X., Ji, P., Wang, P. et al. (2020). *Adv. Energy Mater.* 10: 1903891.

74 Adam, A., Suliman, M.H., Dafalla, H. et al. (2018). *ACS Sustainable Chem. Eng.* 6: 11414–11423.

75 Zhang, Y., Yang, J., Dong, Q. et al. (2018). *ACS Appl. Mater. Interfaces* 10: 26258–26263.

76 Zhu, Y.-P., Xu, X., Su, H. et al. (2015). *ACS Appl. Mater. Interfaces* 7: 28369–28376.

77 Adam, A., Suliman, M.H., Siddiqui, M.N. et al. (2018). *ACS Appl. Mater. Interfaces* 10: 29407–29416.

78 Lv, X., Ren, J., Wang, Y. et al. (2019). *ACS Sustainable Chem. Eng.* 7: 8993–9001.

79 Miao, M., Hou, R., Liang, Z. et al. (2018). *J. Mater. Chem. A* 6: 24107–24113.

80 Heine, T. (2015). *Acc. Chem. Res.* 48: 65–72.

81 Hinnemann, B., Moses, P.G., Bonde, J. et al. (2005). *J. Am. Chem. Soc.* 127: 5308–5309.

82 Li, W., Liu, G., Li, J. et al. (2019). *Appl. Surf. Sci.* 498: 143869.

83 Jaramillo, T.F., Jørgensen, K.P., Bonde, J. et al. (2007). *Science* 317: 100.

84 An, Y.-R., Fan, X.-L., Luo, Z.-F., and Lau, W.-M. (2017). *Nano Lett.* 17: 368–376.

85 Kong, D., Wang, H., Cha, J.J. et al. (2013). *Nano Lett.* 13: 1341–1347.

86 Chen, Z., Cummins, D., Reinecke, B.N. et al. (2011). *Nano Lett.* 11: 4168–4175.

87 Li, Y., Wang, H., Xie, L. et al. (2011). *J. Am. Chem. Soc.* 133: 7296–7299.

88 Tang, Q. and Jiang, D.-e. (2016). *ACS Catal.* 6: 4953–4961.

89 Voiry, D., Salehi, M., Silva, R. et al. (2013). *Nano Lett.* 13: 6222–6227.

90 Hou, X., Zhou, H., Zhao, M. et al. (2020). *ACS Sustainable Chem. Eng.* 8: 5724–5733.

91 Huang, H., Huang, W., Yang, Z. et al. (2017). *J. Mater. Chem. A* 5: 1558–1566.

92 Kong, D., Cha, J.J., Wang, H. et al. (2013). *Energy Environ. Sci.* 6: 3553–3558.

93 Jiang, N., Tang, Q., Sheng, M. et al. (2016). *Catal. Sci. Technol.* 6: 1077–1084.

94 Feng, J.X., Wu, J.Q., Tong, Y.X., and Li, G.R. (2018). *J. Am. Chem. Soc.* 140: 610–617.

95 An, Y., Huang, B., Wang, Z. et al. (2017). *Dalton Trans.* 46: 10700–10706.

96 Anantharaj, S., Subhashini, E., Swaathini, K.C. et al. (2019). *Appl. Surf. Sci.* 487: 1152–1158.

97 Anantharaj, S., Kundu, S., and Noda, S. (2020). *J. Mater. Chem. A* 8: 4174–4192.

98 Wang, F., Li, Y., Shifa, T.A. et al. (2016). *Angew. Chem. Int. Ed.* 55: 6919–6924.

99 Cabán-Acevedo, M., Stone, M.L., Schmidt, J.R. et al. (2015). *Nat. Mater.* 14: 1245–1251.

100 Dutta, B., Wu, Y., Chen, J. et al. (2019). *ACS Catal.* 9: 456–465.

101 Xia, C., Liang, H., Zhu, J. et al. (2017). *Adv. Energy Mater.* 7: 1602089.

102 Jasion, D., Barforoush, J.M., Qiao, Q. et al. (2015). *ACS Catal.* 5: 6653–6657.

103 Miao, R., Dutta, B., Sahoo, S. et al. (2017). *J. Am. Chem. Soc.* 139: 13604–13607.

104 Xu, X., Ge, Y., Wang, M. et al. (2016). *ACS Appl. Mater. Interfaces* 8: 18036–18042.

105 Chen, Y., Zhang, J., Guo, P. et al. (2018). *ACS Appl. Mater. Interfaces* 10: 27787–27794.

106 Jin, H., Liu, X., Vasileff, A. et al. (2018). *ACS Nano* 12: 12761–12769.

107 Liu, B., He, B., Peng, H.-Q. et al. (2018). *Adv. Sci.* 5: 1800406.

108 Chen, Z., Song, Y., Cai, J. et al. (2018). *Angew. Chem. Int. Ed.* 57: 5076–5080.

109 Sun, K., Zhang, T., Tan, L. et al. (2020). *ACS Appl. Mater. Interfaces* 12: 29357–29364.

110 Wang, C., Lv, X., Zhou, P. et al. (2020). *ACS Appl. Mater. Interfaces* 12: 29153–29161.

111 Tang, C., Zhang, H., Xu, K. et al. (2019). *J. Mater. Chem. A* 7: 18030–18038.

112 Ma, Y., Chen, M., Geng, H. et al. (2020). *Adv. Funct. Mater.* 30: 2000561.

113 Huang, J., Wang, J., Xie, R. et al. (2020). *J. Mater. Chem. A* 8: 19879–19886.

114 Song, H.J., Sung, M.-C., Yoon, H. et al. (2019). *Adv. Sci.* 6: 1802135.

115 Gong, M., Wang, D.-Y., Chen, C.-C. et al. (2016). *Nano Res.* 9: 28–46.

116 Zhao, Y., Chang, C., Teng, F. et al. (2017). *Adv. Energy Mater.* 7: 1700005.

117 Jin, Y., Wang, H., Li, J. et al. (2016). *Adv. Mater.* 28: 3785–3790.

118 Shu, C., Kang, S., Jin, Y. et al. (2017). *J. Mater. Chem. A* 5: 9655–9660.

119 Gao, X., Zhang, H., Li, Q. et al. (2016). *Angew. Chem. Int. Ed.* 55: 6290–6294.

120 Zhu, Y., Lin, Q., Zhong, Y. et al. (2020). *Energy Environ. Sci.* 13: 3361–3392.

121 Zheng, T., Sang, W., He, Z. et al. (2017). *Nano Lett.* 17: 7968–7973.

122 Swaminathan, J., Subbiah, R., and Singaram, V. (2016). *ACS Catal.* 6: 2222–2229.

123 Li, Y.H., Liu, P.F., Pan, L.F. et al. (2015). *Nat. Commun.* 6: 8064.

124 Zhang, T., Wu, M.-Y., Yan, D.-Y. et al. (2018). *Nano Energy*. 43: 103–109.

125 Ling, T., Yan, D.-Y., Wang, H. et al. (2017). *Nat. Commun.* 8: 1509.

126 Li, L., Feng, X., Nie, Y. et al. (2015). *ACS Catal.* 5: 4825–4832.

127 Zhang, L., Liu, P.F., Li, Y.H. et al. (2018). *ChemSusChem* 11: 1020–1024.

128 Li, L., Zhang, T., Yan, J. et al. (2017). *Small* 13: 1700441–1700447.

129 Xiao, Z., Wang, Y., Huang, Y.-C. et al. (2017). *Energy Environ. Sci.* 10: 2563–2569.

130 Yu, X., Yu, Z.-Y., Zhang, X.-L. et al. (2020). *Nano Energy*. 71: 104652–104659.

131 Geng, S., Liu, Y., Yu, Y.S. et al. (2019). *Nano Res.* 13: 121–126.

132 Zeng, L., Zhou, K., Yang, L. et al. (2018). *ACS Appl. Energy Mater.* 1: 6279–6287.

133 Dalai, N., Mohanty, B., Mitra, A., and Jena, B. (2019). *ChemistrySelect* 4: 7791–7796.

134 Gu, J., Zhang, C., Du, Z., and Yang, S. (2019). *Small* 15: e1904587.

135 Aqueel Ahmed, A.T., Pawar, S.M., Inamdar, A.I. et al. (2019). *Adv. Mater. Interfaces* 7: 1901515–1901525.

136 Huang, X., Zheng, H., Lu, G. et al. (2018). *ACS Sustainable Chem. Eng.* 7: 1169–1177.

137 Chen, Y., Dong, C., Zhang, J. et al. (2018). *J. Mater. Chem. A* 6: 8430–8440.

138 Ling, T., Zhang, T., Ge, B. et al. (2019). *Adv. Mater.* 31: e1807771.

139 Zhang, H., Li, X., Hähnel, A. et al. (2018). *Adv. Funct. Mater.* 28: 1706847–1706856.

140 Chen, G., Wang, T., Zhang, J. et al. (2018). *Adv. Mater.* 30: 1803694–1809700.

141 Wang, P., Qi, J., Chen, X. et al. (2020). *ACS Appl. Mater. Interfaces* 12: 4385–4395.

142 Gao, X., Zhao, Y., Dai, K. et al. (2020). *Chem. Eng. J.* 384: 123373.

143 Sun, H., Li, J.-G., Lv, L. et al. (2019). *J. Power Sources* 425: 138–146.

144 Wang, Y., Wang, T., Zhang, R. et al. (2020). *Inorg. Chem.* 59: 9491–9495.

145 Grimaud, A., Hong, W.T., Shao-Horn, Y., and Tarascon, J.M. (2016). *Nat. Mater.* 15: 121–126.

146 Song, J., Wei, C., Huang, Z.F. et al. (2020). *Chem. Soc. Rev.* 49: 2196–2214.

147 Man, I.C., Su, H.Y., Calle-Vallejo, F. et al. (2011). *ChemCatChem* 3: 1159–1165.

148 Montoya, J.H., Seitz, L.C., Chakthranont, P. et al. (2016). *Nat. Mater.* 16: 70–81.

149 Grimaud, A., Diaz-Morales, O., Han, B. et al. (2017). *Nat. Chem.* 9: 457–465.

150 Surendranath, Y., Kanan, M.W., and Nocera, D.G. (2010). *J. Am. Chem. Soc.* 132: 16501–16509.

151 Fierro, S., Nagel, T., Baltruschat, H., and Comninellis, C. (2007). *Electrochim. Commun.* 9: 1969–1974.

152 Kulkarni, A., Siahrostami, S., Patel, A., and Norskov, J.K. (2018). *Chem. Rev.* 118: 2302–2312.

153 Nong, H.N., Falling, L.J., Bergmann, A. et al. (2020). *Nature* 587: 408–413.

154 Burke, M.S., Enman, L.J., Batchellor, A.S. et al. (2015). *Chem. Mater.* 27: 7549–7558.

155 Burke, M.S., Zou, S., Enman, L.J. et al. (2015). *J. Phys. Chem. Lett.* 6: 3737–3742.

156 Stern, L.A. and Hu, X. (2014). *Faraday Discuss.* 176: 363–379.

157 McCrory, C.C., Jung, S., Peters, J.C., and Jaramillo, T.F. (2013). *J. Am. Chem. Soc.* 135: 16977–16987.

158 Huang, J., Li, Y., Zhang, Y. et al. (2019). *Angew. Chem. Int. Ed.* 58: 17458–17464.

159 Diaz-Morales, O., Ferrus-Suspedra, D., and Koper, M.T.M. (2016). *Chem. Sci.* 7: 2639–2645.

160 Li, L.-F., Li, Y.-F., and Liu, Z.-P. (2020). *ACS Catal.* 10: 2581–2590.

161 Li, Y.-F. and Selloni, A. (2014). *ACS Catal.* 4: 1148–1153.

162 Klaus, S., Cai, Y., Louie, M.W. et al. (2015). *J. Phys. Chem. C* 119: 7243–7254.

163 Trotochaud, L., Young, S.L., Ranney, J.K., and Boettcher, S.W. (2014). *J. Am. Chem. Soc.* 136: 6744–6753.

164 Zhang, F., Wang, W., Li, Z. et al. (2020). *Mol. Catal.* 493: 111082–111089.

165 Jin, Y., Huang, S., Yue, X. et al. (2018). *ACS Catal.* 8: 2359–2363.

166 Yan, J., Kong, L., Ji, Y. et al. (2019). *Nat. Commun.* 10: 2149.

167 Dou, Y., He, C.-T., Zhang, L. et al. (2020). *Cell Rep. Phys. Sci.* 1: 100077–100090.

168 Diaz-Morales, O., Ledezma-Yanez, I., Koper, M.T.M., and Calle-Vallejo, F. (2015). *ACS Catal.* 5: 5380–5387.

169 Jiang, J., Sun, F., Zhou, S. et al. (2018). *Nat. Commun.* 9: 2885.

170 Favaro, M., Drisdell, W.S., Marcus, M.A. et al. (2017). *ACS Catal.* 7: 1248–1258.

171 Zhang, Z., Zhang, T., and Lee, J.Y. (2018). *ACS Appl. Nano Mater.* 1: 751–758.

172 Qiao, X., Kang, H., Li, Y. et al. (2020). *ACS Appl. Mater. Interfaces* 12: 36208–36219.

173 Luan, C., Liu, G., Liu, Y. et al. (2018). *ACS Nano* 12: 3875–3885.

174 Cheng, Y. and Jiang, S.P. (2015). *Prog. Nat. Sci.: Mater. Int.* 25: 545–553.

175 Yao, Y., Xu, Z., Cheng, F. et al. (2018). *Energy Environ. Sci.* 11: 407–416.

176 Liao, C., Yang, B., Zhang, N. et al. (2019). *Adv. Funct. Mater.* 29: 1904020–1904030.

177 Favaro, M., Yang, J., Nappini, S. et al. (2017). *J. Am. Chem. Soc.* 139: 8960–8970.

178 Bergmann, A., Jones, T.E., Martinez Moreno, E. et al. (2018). *Nat. Catal.* 1: 711–719.

179 Moysiadou, A., Lee, S., Hsu, C.S. et al. (2020). *J. Am. Chem. Soc.* 142: 11901–11914.

180 Chou, N.H., Ross, P.N., Bell, A.T., and Tilley, T.D. (2011). *ChemSusChem* 4: 1566–1569.

181 Han, L., Dong, S., and Wang, E. (2016). *Adv. Mater.* 28: 9266–9291.

182 Sidhureddy, B., Dondapati, J.S., and Chen, A. (2019). *Chem. Commun.* 55: 3626–3629.

183 Pan, S., Mao, X., Yu, J. et al. (2020). *Inorg. Chem. Front.* 7: 3327–3339.

184 Jin, H., Mao, S., Zhan, G. et al. (2017). *J. Mater. Chem. A* 5: 1078–1084.

185 Chen, L., Zhang, H., Chen, L. et al. (2017). *J. Mater. Chem. A* 5: 22568–22575.

186 Zhou, Q., Chen, Y., Zhao, G. et al. (2018). *ACS Catal.* 8: 5382–5390.

187 Raj, S., Anantharaj, S., Kundu, S., and Roy, P. (2019). *ACS Sustainable Chem. Eng.* 7: 9690–9698.

188 Su, P., Ma, S., Huang, W. et al. (2019). *J. Mater. Chem. A* 7: 19415–19422.

189 He, L., Liu, J., Hu, B. et al. (2019). *J. Power Sources* 414: 333–344.

190 Zhang, S., Yu, T., Wen, H. et al. (2020). *Chem. Commun.* 56: 15387–15405.

191 Al-Mamun, M., Zhu, Z., Yin, H. et al. (2016). *Chem. Commun.* 52: 9450–9453.

192 Kou, Y., Liu, J., Li, Y. et al. (2018). *ACS Appl. Mater. Interfaces* 10: 796–805.

193 Chen, P., Zhou, T., Wang, S. et al. (2018). *Angew. Chem. Int. Ed.* 57: 15471–15475.

194 Wang, L., Lin, C., Huang, D. et al. (2014). *ACS Appl. Mater. Interfaces* 6: 10172–10180.

195 Zhuang, L., Ge, L., Yang, Y. et al. (2017). *Adv. Mater.* 29: 1606793–1160679.

196 Zhuang, L., Jia, Y., He, T. et al. (2018). *Nano Res.* 11: 3509–3518.

197 Lu, X. and Zhao, C. (2013). *J. Mater. Chem. A* 1: 12053–12059.

198 Mallón, L., Romero, N., Jiménez, A. et al. (2020). *Catal. Sci. Technol.* 10: 4513–4521.

199 Zou, S., Burke, M.S., Kast, M.G. et al. (2015). *Chem. Mater.* 27: 8011–8020.

200 Lyons, M.E. and Brandon, M.P. (2009). *Phys. Chem. Chem. Phys.* 11: 2203–2217.

201 Zhang, X., An, L., Yin, J. et al. (2017). *Sci. Rep.* 7: 43590.

202 Zhang, S., Gao, H., Huang, Y. et al. (2018). *Environ. Sci.: Nano* 5: 1179–1190.

203 Niu, S., Jiang, W.J., Wei, Z. et al. (2019). *J. Am. Chem. Soc.* 141: 7005–7013.

204 Yoon, K.-Y., Ahn, H.-J., Kwak, M.-J. et al. (2016). *J. Mater. Chem. A* 4: 18730–18736.

205 Yin, Y., Zhang, X., and Sun, C. (2018). *Prog. Nat. Sci.: Mater. Int.* 28: 430–436.

206 Han, S., Liu, S., Yin, S. et al. (2016). *Electrochim. Acta* 210: 942–949.

207 Liu, X., Cui, S., Sun, Z. et al. (2016). *J. Phys. Chem. C* 120: 831–840.

208 Pawar, S.M., Pawar, B.S., Hou, B. et al. (2017). *J. Mater. Chem. A* 5: 12747–12751.

209 Xiong, X., You, C., Liu, Z. et al. (2018). *ACS Sustainable Chem. Eng.* 6: 2883–2887.

210 Huan, T.N., Rousse, G., Zanna, S. et al. (2017). *Angew. Chem. Int. Ed.* 56: 4792–4796.

211 Valdés, Á., Qu, Z.W., Kroes, G.J. et al. (2008). *J. Phys. Chem. C* 112: 9872–9879.

212 García-Mota, M., Vojvodic, A., Metiu, H. et al. (2011). *ChemCatChem* 3: 1607–1611.

213 Kumbhar, V.S., Lee, H., Lee, J., and Lee, K. (2019). *Carbon Resour. Convers.* 2: 242–255.

214 Huynh, M., Bediako, D.K., and Nocera, D.G. (2014). *J. Am. Chem. Soc.* 136: 6002–6010.

215 Huynh, M., Shi, C., Billinge, S.J., and Nocera, D.G. (2015). *J. Am. Chem. Soc.* 137: 14887–14904.

216 Morgan Chan, Z., Kitchev, D.A., Nelson Weker, J. et al. (2018). *Proc. Natl. Acad. Sci. U.S.A.* 115: E5261–E5268.

217 Liu, P.-P., Zheng, Y.-Q., Zhu, H.-L., and Li, T.-T. (2019). *ACS Appl. Nano Mater.* 2: 744–749.

218 Jin, K., Chu, A., Park, J. et al. (2015). *Sci. Rep.* 5: 10279.

219 Chandrasekaran, S., Kim, E.J., Chung, J.S. et al. (2016). *J. Mater. Chem. A* 4: 13271–13279.

220 Gonçalves, J.M., Ireno da Silva, M., Angnes, L., and Araki, K. (2020). *J. Mater. Chem. A* 8: 2171–2206.

221 Cui, Y., Xue, Y., Zhang, R. et al. (2019). *J. Mater. Chem. A* 7: 21911–21917.

222 Lee, W.H., Ko, Y.J., Kim, J.Y. et al. (2020). *Chem. Commun.* 56: 12687–12697.

223 Zhu, C., Shi, Q., Feng, S. et al. (2018). *ACS Energy Lett.* 3: 1713–1721.

224 Chen, P., Zhou, T., Xing, L. et al. (2017). *Angew. Chem. Int. Ed.* 56: 610–614.

225 Zheng, Y., Jiao, Y., Zhu, Y. et al. (2017). *J. Am. Chem. Soc.* 139: 3336–3339.

226 Hou, Y., Qiu, M., Kim, M.G. et al. (2019). *Nat. Commun.* 10: 1392.

227 Li, Y., Wu, Z.S., Lu, P. et al. (2020). *Adv. Sci.* 7: 1903089.

228 Fei, H., Dong, J., Feng, Y. et al. (2018). *Nat. Catal.* 1: 63–72.

229 Ying, Y., Luo, X., Qiao, J., and Huang, H. (2020). *Adv. Funct. Mater.* 31: 2007423–2007447.

230 Bai, L., Hsu, C.S., Alexander, D.T.L. et al. (2019). *J. Am. Chem. Soc.* 141: 14190–14199.

231 Tavakkoli, M., Flahaut, E., Peljo, P. et al. (2020). *ACS Catal.* 10: 4647–4658.

232 Han, X., Ling, X., Yu, D. et al. (2019). *Adv. Mater.* 31: e1905622.

233 Zhu, X.F., Zhang, D.T., Chen, C.J. et al. (2020). *Nano Energy.* 71: 104597–104607.

234 Yin, J., Jin, J., Lin, H. et al. (2020). *Adv. Sci.* 7: 1903070.

235 Peng, X., Pi, C., Zhang, X. et al. (2019). *Sustain. Energy Fuels* 3: 366–381.

236 Dutta, A. and Pradhan, N. (2017). *J. Phys. Chem. Lett.* 8: 144–152.

237 Jin, S. (2017). *ACS Energy Lett.* 2: 1937–1938.

238 Wygant, B.R., Kawashima, K., and Mullins, C.B. (2018). *ACS Energy Lett.* 3: 2956–2966.

239 Stern, L.-A., Feng, L., Song, F., and Hu, X. (2015). *Energy Environ. Sci.* 8: 2347–2351.

240 Chen, P., Xu, K., Fang, Z. et al. (2015). *Angew. Chem. Int. Ed.* 54: 14710–14714.

241 Xu, J., Li, J., Xiong, D. et al. (2018). *Chem. Sci.* 9: 3470–3476.

242 Li, W., Xiong, D., Gao, X., and Liu, L. (2019). *Chem. Commun.* 55: 8744–8763.

243 Ghoshal, S., Zaccarine, S., Anderson, G.C. et al. (2019). *ACS Appl. Energy Mater.* 2: 5568–5576.

244 Zheng, W., Liu, M., and Lee, L.Y.S. (2020). *ACS Catal.* 10: 81–92.

245 Asthagiri, A. and Janik, M.J. (2014). *Computational Catalysis*. RSC Publishing.

246 Soriano-López, J., Schmitt, W., and García-Melchor, M. (2018). *Curr. Opin. Electrochem.* 7: 22–30.

247 Abild-Pedersen, F. (2016). *Catal. Today* 272: 6–13.

248 Greeley, J., Jaramillo, T.F., Bonde, J. et al. (2006). *Nat. Mater.* 5: 909–913.

249 Bjorketun, M.E., Bondarenko, A.S., Abrams, B.L. et al. (2010). *Phys. Chem. Chem. Phys.* 12: 10536–10541.

250 Haber, J.A., Cai, Y., Jung, S. et al. (2014). *Energy Environ. Sci.* 7: 682–688.

251 Ge, L., Yuan, H., Min, Y. et al. (2020). *J. Phys. Chem. Lett.* 11: 869–876.

252 Chatenet, M., Benziger, J., Inaba, M. et al. (2020). *J. Power Sources* 451: 227635–227638.

253 Chen, J.G., Jones, C.W., Linic, S., and Stamenkovic, V.R. (2017). *ACS Catal.* 7: 6392–6393.

254 Voiry, D., Chhowalla, M., Gogotsi, Y. et al. (2018). *ACS Nano* 12: 9635–9638.

255 Bird, M.A., Goodwin, S.E., and Walsh, D.A. (2020). *ACS Appl. Mater. Interfaces* 12: 20500–20506.

256 Anantharaj, S. and Kundu, S. (2019). *ACS Energy Lett.* 4: 1260–1264.

257 Zheng, W., Liu, M., and Lee, L.Y.S. (2020). *ACS Energy Lett.* 5: 3260–3264.

